ROYAL INSTITUTE
OF TECHNOLOGY

Surface studies on α–sapphire for potential use in GaN epitaxial growth

Licentiate thesis

BJÖRN AGNARSSON

Microelectronics and Applied Physics
School for Information and Communication Technology
Royal Institute of Technology

Stockholm 2009

Surface studies on α–sapphire for potential use in GaN epitaxial growth

Materials Physics School of Information and Communication Technology

Royal Institute of Technology

TRITA-ICT/MAP AVH Report 2009:03
ISSN 1653-7610
ISRN KTH/ICT-MAP/AVH-2009:03-SE
ISBN 978-91-7415-286-9

Sammanfattning

Denna Licentiatavhandling sammanfattar det arbete som utförts av författaren under åren 2004 till 2008 vid Islands Universitet och Kungliga Tekniska Högskolan (KTH) i Sverige. Syftet med projektet var att undersöka safirs yta (?-Al2O3), både av grundvetenskapliga och tillämpade skäl, för användning som substrat för GaN-tillväxt med molekylstråleepitaxi.

Avhandlingen beskriver först några olika analysmetoder som används inom ytfysiken; deras fysikaliska grundprinciper, experimentella genomförande och vilken information de kan ge. Vidare beskrivs några metoder för att preparera/förbereda safirytor för användning som substrat för epitaxiell tillväxt av GaN.

Avhandlingen bygger huvudsakligen på tre publicerade (eller snart offentliggjorda) artiklar.

Den första artikeln är inriktad på tillväxt av tunna AlN-lager på safir som bufferlager för epitaxiell tillväxt av GaN eller en liknande III-V material. Två typer av safirsubstrat (rekonstruerade och icke-rekonstruerade) exponerades för ammoniak som ledde till bildandet av AlN på ytan. Verkningsgraden av AlN bildning (nitrideringseffektivitet) för de två ytorna jämfördes sedan som en funktion av substrattemperatur med fotoelektronspektroskopi och lågenergielektrondiffraktion. Den rekonstruerade ytan visade en betydlig högre nitriderings-effektivitet än den icke-rekonstruerade ytan.

I den andra artikeln studerades effekten av olika värmebehandlingar på safirs ytmorfologi, och därmed dess förmåga att fungera som substrat för GaN tillväxt. Atomkraftsmikroskopi, röntgendiffraktionsanalys och ellipsometrimätningar visade att värmning i H2-gas och därefter värmning vid 1300 °C i O2 under 11 timmar, leder till hög kvalitet och atomärt plana safirytor som lämpar sig för epitaxiell III-V tillväxt.

Det tredje papperet beskriver effekten av argonsputtring för rengöring GaN ytor och möjligheten att använda indium som en form av tensid för att skapa en ren och stökiometrisk GaN yta. Mjuksputtring, följt av deponering av 2 ML indium och värmebehandling vid ca 500 °C resulterar i välordnade och rena GaN-ytor. Hårdsputtring, däremot, skapar vakanser och metalliskt gallium, som inte kan tas bort med hjälp av indium.

Abstract

This Licentiate thesis summarizes the work carried out by the author the years 2004 to 2008 at the University of Iceland and the Royal Institute of Technology (KTH) in Sweden. The aim of the project was to investigate the structure of sapphire (?-Al2O3) surfaces, both for pure scientific reasons and also for potential use as substrate for GaN-growth by molecular beam epitaxy.

More generally the thesis describes some surface science methods used for investigating the substrates; the general physical back ground, the experimental implementation and what information they can give. The described techniques are used for surface analysis on sapphire substrates which have been treated variously in order to optimize them for use as templates for epitaxial growth of GaN or related III-V compounds.

The thesis is based on three published (or submitted) papers.

The first paper focuses on the formation a thin AlN layer on sapphire, which may act as a buffer layer for potential epitaxial growth of GaN or any related III-V materials. Two types of sapphire substrates (reconstructed and non-reconstructed) were exposed to ammonia resulting in the formation of AlN on the surface. The efficiency of the AlN formation (nitridation efficiency) for the two surfaces was then compared as a function of substrate temperature through photoelectron spectroscopy and low electron energy diffraction. The reconstructed surface showed a much higher nitridation efficiency than the non-reconstructed surface.

In the second paper, the affect of different annealing processes on the sapphire morphology, and thus its capability to act as a template for GaN growth, was studied. Atomic force microscopy, X-ray diffraction analysis together with ellipsometry measurements showed that annealing in H2 ambient and subsequent annealing at 1300 °C in O2 for 11 hours resulted in high quality and atomically flat sapphire surface suitable for III-V epitaxial growth.

The third paper describes the effect of argon sputtering on cleaning GaN surfaces and the possibility of using indium as surfactant for establishing a clean and stoichiometric GaN surface, after such sputtering. Soft sputtering, followed by deposition of 2 ML of indium and subsequent annealing at around 500 °C resulted in a well ordered and clean GaN surface while hard sputtering introduced defects and incorporated both metallic gallium and indium in the surface.

Acknowledgment

All the work presented here was carried out between 2004 and 2008 either at the Royal Institute of Technology (KTH), Sweden, under the supervision of Dr. Mats Göthelid and Professor Ulf Karlsson or at the University of Iceland under the supervision of Dr. Sveinn Ólafsson and Professor Hafliði P. Gíslason. I would like to thank all of them for making it possible for me to carry out my work in both Sweden and Iceland and for showing tremendous patience and understanding in sometimes difficult circumstances.

I would of course also like to thank them for their educational contribution and for being responsible for creating a stimulating working environment. It is my hope that the my project has helped in bringing the two institutions a bit closer to each other and that it has helped in establishing a foundation for future research cooperation between the two institutes. I would also like to thank all the persons that have helped me on my way towards this degree, how small or big their contribution might have been. These include all the students I have had the pleasure to work with or alongside, the administration and maintenance staff of both institutions and the staff at MaxLab in Lund.

Last but not least, I thank my family for their support and understanding throughout my studies.

Contents

List of Figures

List of Tables

List of Publications

This thesis is based on the following papers and manuscripts. In the text, these publications are referred to as [P1].

[P1] B. Agnarsson, M. Göthelid, S. Olafsson, H.P. Gislason and U.O. Karlsson, "Influence of initial surface reconstruction on nitratdation of Al_2O_3 (0001) using low pressure ammonia," in *Journal of Applied Physics*, vol. 101, 013519, 2007.

[P2] BingCui Qi, B. Agnarsson, K. Jonsson, S. Olafsson and H.P. Gislason, "Characterisation of high-temperature annealing effects on $\alpha - Al_2O_3(0001)$ substrates," in *Journal of Physics, Conference Series*, vol. 1000, 042020, 2008.

[P3] B. Agnarsson, B. Qi, K. Szamota-Leandersson, S. Olafsson, M. Göthelid, "Investigation on the role of indium in the removal of metallic gallium from soft and hard sputtered GaN(0001) surfaces," Manuscript in preparation.

Chapter 1

Introduction

In the spring 2003 the University of Iceland (UI) received a molecular beam epitaxy system (MBE) from the Royal Institute of Technology, Stockholm (KTH). On top of this generous gift, KTH also decided to start a collaboration with UI and financially support a Ph.D. student to start a new line of solid state physics research at UI by using the MBE system to produce and investigate nitride semiconducting compound materials. Initially the plan was to study GaN, MnN and InN, which are very distinctive wide band-gap semiconducting materials, with respect to possible application in the solar cell industry.

The reason for our interest in nitride compounds is mainly two fold. Firstly from scientific point of view because lots of nitride compounds are yet to be fully understood and many of them like InN, GaN and MnN look promising for future applications like solar-cells and spintronics. Secondly because many groups in Sweden and especially at KTH have been focusing on nitride compounds and it would thus be good to contribute to their work and establish some cooperation in this field.

In recent years, researchers have been increasingly interested in nitride related semiconducting materials, such as GaN, InN and AlN. Due to the wide direct bandgap of these materials, they are considered ideal candidates for light emission applications such as light emitting diodes (LED) and lasers and today III-V semiconductors are indispensable in optoelectronic devices such as semiconductor lasers used in optical communication systems. Likewise, this class of materials is dominant in key high frequency electronic components for wireless communication systems. Other applications of nitride based materials include spintronic devices, high frequency communication devices and other things that take advantage of the wide bandgap properties.

Efficient red and yellow light-emitting devices have existed for some years but it was not until the high power GaN blue-LED and the green InGaN were developed

that full colour (red, green, blue) displays became available. However, even though nitride related, blue light emitting devices have been around for some time, there is still some distance to go before these devices become as powerful as their counterparts in the red and green part of the spectra and research is still ongoing to improve this [5].

Recent studies on the bandgap properties of InN seem to suggest that it has a bandgap below 1 eV instead of the previously commonly accepted value of around 2 eV [1]. The majority of the investigations that reported band gap energies in this range were carried out on samples grown by sputtering techniques and were characterised as having a polycrystalline structure. The drastic improvement in the growth techniques, especially in molecular beam epitaxy (MBE) and metalorganic vapour phase epitaxy (MOVPE), has recently led to the availability of very high quality material. As a consequence the range of wavelengths that can be accessed by alloying InN (0.7 eV) with GaN (3.4 eV) has been significantly extended (see figure 1.1). Indeed $In_{1-x}Ga_xN$ has the widest range of direct gap of any compound semiconductors, ranging from 0.7 eV (for $x = 1$) to 3.4 eV (for $x = 0$), which can be utilised in optoelectronic device applications over a wide range of wavelengths from ultraviolet to infrared. This would make it ideal for applications in data storage, medical (photo dynamic therapy and surgery), environmental (solar cells, sensors of obnoxious gases), security (terahertz (THz) emitters and detectors) and communications (optical amplifiers, lasers and detectors) fields.

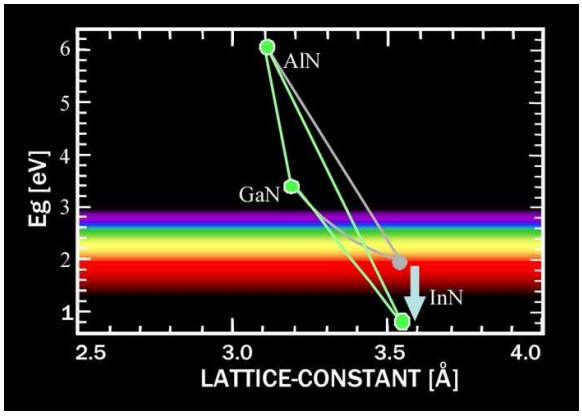

Figure 1.1. Energy gap of different compound semiconductors as a function of lattice constant. Figure is taken from the Matsuoka Laboratory webpage at Tohoku University.

Wide band gap semiconductor materials extend the field of semiconductor applications to the limits where conventional semiconductors such as Si and GaAs fail.

They can emit light at shorter wavelengths and can operate at higher temperatures all because of larger band gap, higher thermal conductivity and chemical inertness. In my work we decided to grow GaN on a sapphire substrate mainly because GaN is a relatively well studied wide-bandgap-semiconductor. Furthermore, GaN based nitride semiconductors have several advantages over other wide bandgap semiconductors since they can be doped both p and n-type, they have direct bandgaps, they form heterostructures suitable for device applications and can relatively easily be epitaxially grown on a number of substrates. How ever it soon became evident that this ambitious plan would not be realised unless some basic fundamental questions regarding the fabrication method would be answered first. The main focus thus went on the sapphire substrate itself, its atomic arrangement, surface morphology and some of its basic geometrical properties.

This thesis is based on three published papers. The first focuses on nitridation efficiency on unreconstructed and reconstructed sapphire substrates. The second paper focuses on the effect of annealing on the morphology of sapphire surface and crystallographic properties. Finally, the third paper describes a method to remove metallic Gallium from GaN substrate after soft sputtering by using indium as surfactant.

Even though the principles of nitride semiconductor devices are quite well understood from a theoretical point of view, these devices will not become a reality unless some major technical difficulties are overcome. One of the biggest problems concern the growth of high quality nitride single crystals. In order to grow a single-crystal nitride semiconductor one needs a substrate with a similar lattice parameter as the desired semiconductor crystal. Finding such a substrate for nitride semiconductors has been difficult and the best candidates are either too expensive or to hard to come by in order for them to be a feasible choice for mass manufacturing. Sapphire (α-Al_2O_3), however is a substrate that is cheap, hard, transparent in the visible spectrum, thermally stable and it is available with very high crystal quality. All these properties would make it ideal as substrate for growing GaN. However, the disadvantage with sapphire is its relatively large mismatch in lattice constants (14%) and thermal coefficient (32%) compared to GaN which induce stress-related defects at the interface which act to lower the crystal quality of the overlayer. By optimising the growth procedure for GaN on sapphire, it is hoped that this problem may be overcome and that sapphire may one day be used as substrate for growing high quality GaN. One of the first questions that arise is how the quality and morphology of the sapphire itself effects the growth of the GaN. It has been shown in various articles that this is in fact one of the key issues when it comes to growing high quality GaN crystals[2, 3, 4]. One way of improving the growth is to *nitride* the sapphire surface prior to growth by exposing the substrate to nitrogen. The purpose of the nitridation process is to lower the lattice mismatch by converting the topmost layers to AlN, which has a much smaller lattice mismatch (3%) compared to GaN than sapphire, thus reducing interfacial defects and making it easier

to grow hight quality GaN epilayers. The mechanism of the nitridation process is not well understood which makes it even more interesting as a study. AlN/Al_2O_3 systems are also interesting with respect to the possibility of using high quality bulk AlN and Al-O-N for structural and optical applications [5]. The issue of sapphire nitridation and morphology are raised and discussed in papers [P1] and [P2] of this thesis.

As mentioned before, studies on GaN and similar compounds are an increasing field in science and with it comes the need to be able to obtain a clean and well ordered nitride-compound surfaces. The most widely used method for obtaining clean GaN surfaces is by argon sputtering. Unfortunately, there is a side-effect to this method which results in the formation of metallic gallium on the surface after sputtering and successive annealing. This poses a problem for additional growth on that particular surface. A novel way to clean GaN without introducing surface defects is thus needed and very important towards taking the next step in making GaN-related heterosctructures. There have been indications that indium may act as a surfactant in GaN growth and help rearrange atoms in such a way that it results in a higher crystal quality [6, 7, 8] and hence might also be able to help to arrange the surface atoms in such a way that metallic gallium droplets would not form. Afterwards the remaining indium could safely be annealed away leaving a well ordered and clean GaN surface behind. This issue is studied in the unpublished report on In as a possible cleaner for GaN [P3].

Chapter 2

Property of the materials under investigation

2.1 Crystals

Solid state physics is largely concerned with crystals, which are solids whose atoms are arranged in a periodic array. The simple geometric regularity of crystalline matter is probably the single most important feature in modern application of solid state devices. The regularity ensures that scientists are able to manipulate and control matter in order to obtain desired property. The regular periodicity also enables theorists make certain simplification to otherwise very complex systems, which helps them to construct useful physical models to describe electrical and optical behaviour of solid state matter. Crystals are thus the key to understanding matter and also for use in technical applications. In my thesis I deal mostly with two-dimensional crystals, that is to say crystal surfaces.

A real crystal is described by an underlying set of lattice points, called the *Bravais lattice*, and a set of atoms or molecules usually referred to as basis [9]. A Bravais lattice is an infinite matrix of points generated by the vectors:

$$\mathbf{R} = \sum n_i \mathbf{a}_i \qquad i = 1, 2, 3 \tag{2.1}$$

Where $\mathbf{a}_i$ are the primitive vectors of the lattice forming the *primitive unit cell* and n_i are integer values. For three dimensions there are fourteen types of Bravais lattices but when categorised according to their symmetry properties, all Bravais lattices and real crystals fall into one of seven groupings - the seven crystal systems [10]. For two dimensions these types are ten and when categorised according to symmetry give five crystal systems [9]. Most of the semiconducting materials are either members of the cubic system or the hexagonal system.

2.2 Reciprocal space

In order to understand wave interaction (electron, photons) with electrons in periodic crystalline structures, it is helpfull to introduce the concept of *reciprocal space* which is nothing else but Fourier space in two or three dimensions. The reciprocal space is also important for understanding the quantum mechanical properties of electrons in periodic potentials and how momentum is conserved in crystals.

The set of plane waves of electrons or photons, with wave-vector $\mathbf{k}$, that has the same periodicity as the Bravais lattice it is interacting with, form the reciprocal lattice. In that case, the wave-vector is denoted by $\mathbf{K}$ and the following relation holds between the points $\mathbf{R}$ of the real lattice and the points $\mathbf{K}$ of the reciprocal lattice:

$$e^{\mathbf{K}\cdot\mathbf{R}} = 1 \tag{2.2}$$

for all $\mathbf{R}$ in the Bravais lattice [11]. So each Bravais lattice in real space is uniquely determined by a Bravais lattice in the reciprocal space and vice versa. Since the direct lattice vectors, $\mathbf{R}$, are described in terms of the primitive unit cell vectors, $\mathbf{a}_i$, the reciprocal lattice vector, $\mathbf{K}$, can be defined in terms of primitive lattice vectors, $\mathbf{b}_i$ in the following manner in three dimensions:

$$\mathbf{b}_1 = 2\pi\frac{\mathbf{a}_2 \times \mathbf{a}_3}{\mathbf{a}_1 \cdot \mathbf{a}_2 \times \mathbf{a}_3} \quad \mathbf{b}_2 = 2\pi\frac{\mathbf{a}_3 \times \mathbf{a}_1}{\mathbf{a}_1 \cdot \mathbf{a}_2 \times \mathbf{a}_3} \quad \mathbf{b}_1 = 2\pi\frac{\mathbf{a}_1 \times \mathbf{a}_2}{\mathbf{a}_1 \cdot \mathbf{a}_2 \times \mathbf{a}_3} \tag{2.3}$$

And in two dimensions:

$$\mathbf{b}_1 = 2\pi\frac{\mathbf{a}_2 \times \hat{\mathbf{n}}}{|\mathbf{a}_1 \times \mathbf{a}_2|} \quad \mathbf{b}_2 = 2\pi\frac{\hat{\mathbf{n}} \times \mathbf{a}_1}{|\mathbf{a}_1 \times \mathbf{a}_2|} \tag{2.4}$$

Where $\hat{\mathbf{n}}$ is the unit vector normal to the surface. Hence in three dimensions the reciprocal vector, $\mathbf{K}$, can be expressed as:

$$\mathbf{K} = h\mathbf{b}_1 + k\mathbf{b}_2 + l\mathbf{b}_1 \tag{2.5}$$

Where the integers h, k and l, which have no common factor, are known as the *Miller indices*.

There is an important relationship between the reciprocal lattice vector, $\mathbf{K}$, and the lattice planes of the corresponding lattice. A lattice plane can be determined by three non-collinear lattice sites. Each of these planes contain infinitely many lattice sites and each of the reciprocal vector is normal to some set of planes in the direct lattice with the length of $\mathbf{K}$ being inversely proportional to the spacing between the planes of the set. The spacing between adjacent lattice planes perpendicular to $\mathbf{K}$ is given by [12]:

$$d_{hkl} = \frac{2\pi}{|\mathbf{K}_{hkl}|} \tag{2.6}$$

So for every reciprocal lattice vector $\mathbf{K}$ there is a set of lattice planes which are normal to it, whose spacing is inversely proportional to the shortest reciprocal lattice vector in the direction of $\mathbf{K}$. It is thus sufficient to specify the Miller indices $(h, k.l)$ (point in reciprocal space) in order to characterise a set of planes in a direct lattice.

2.2.1 Superstructure

Usually when dealing with crystal surfaces, as is the focus in this thesis, it is sufficient to use a two dimensional model to describe the system under investigation. Strictly speaking, all surface regions are three-dimensional but all the symmetry properties are two dimensional. The surface crystallography is thus two dimensional and has to be treated using two dimensional point groups and two dimensional Bravais lattices. The result is ten different point group symmetries and consequently only five two dimensional Bravais lattices [13]. How ever, most experimental probes in surface science such as the ones mentioned in this thesis, have non-negligible penetration depth. This means that the information obtained is related to several atomic layers with the topmost layer being the most dominant one. As a result, in situations where a different periodicity is present in the topmost layer, a surface lattice, called *superlattice*, is superimposed on the basic periodicity of the underlying atomic layers. Using Wood's notation there exists a simple way of expressing superstructures in terms of ratio of the lengths of the primitive translational vectors of the superstructure and those of the substrate unit mesh. If a certain surface, made of element X, is labelled as $X\{hkl\}$, then a reconstruction is given with:

$$\mathbf{a}_1^* = p\mathbf{a}_1 \qquad \mathbf{a}_2^* = q\mathbf{a}_2$$

and the notation is given by:

$$X\{hkl\}(p \times q)$$

If the translational vectors of the substrate and of the superstructure are not parallel, but rotated with respect to each other by angle R° or if a possible centering exists, then the situation is described by:

$$X\{hkl\}(p \times q)R \quad \text{or} \quad X\{hkl\}c(p \times q)R$$

Figure 2.1(a) and 2.1(b) shows different superlattices in real space and in reciprocal space using this notation.

2.3 Sapphire

Sapphire (α-Al_2O_3) has been thoroughly studied with regard to its bulk properties and as substrate for growth of silicon, however very little effort has been put into studies of surface structures and morphology [14, 15]. Due to the high crystalline quality, chemical inertness, hardness, low cost, optical transparency and high thermal coefficients, it has become an important material with applications in optical

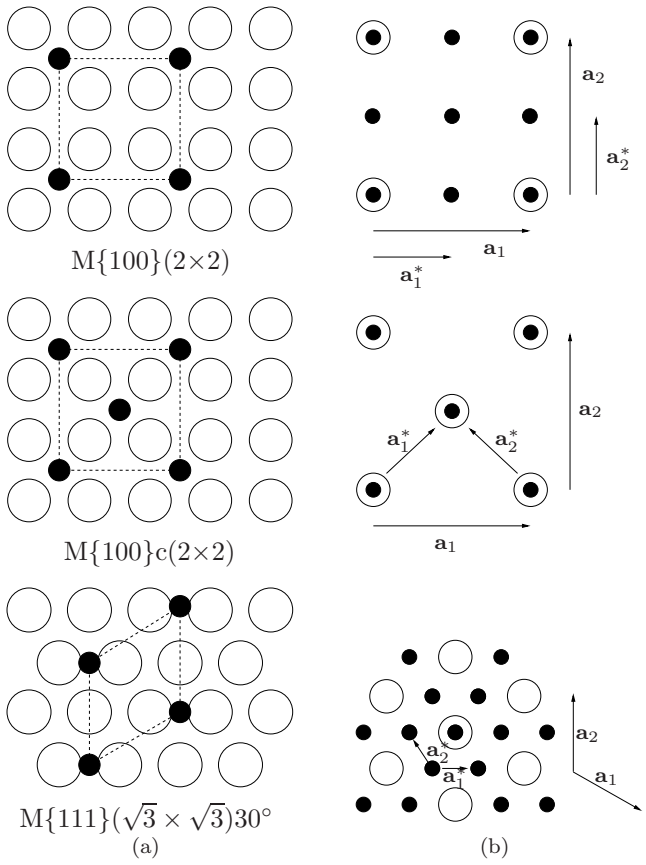

Figure 2.1. Different superlattices in real and reciprocal space. Solid dots represent superstructure and circles represent substrate. (a) Real space. (b) Reciprocal space.

windows, masers and in thin-film microelectronics. α-sapphire has a trigonal crystal symmetry (oxygen atoms form a hexagonal lattice) and is stable at high temperatures (1000 °C) in vacuum and in nitrogen and hydrogen atmospheres. For epitaxial growth the c-plane (0001) has been mostly used but other orientations such as the a-plane and r-plane are also used. In my work only the hexagonal c-plane was used. The crystal structure is corundum type and often represented by hexagonal cell vectors. The atomic arrangements of sapphire is shown in figure 2.2. It is composed of Al^{3+} and O^{2-} ions with the former occupying 2/3 of the octahedral sites and the O^{2+} ions forming a hexagonal close-packed structure (HCP).

Sapphire is optically transparent between 260 and 5000 nm and in the visible

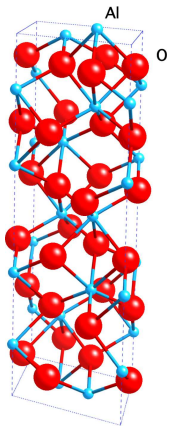

Figure 2.2. Crystal structure of α-sapphire. The dotted area represents the hexagonal unit cell and different coloured circles represent the two different atom species.

range the refractive index is between 1.75-1.78 [16]. This transparency together with its low refractive index makes sapphire especially suitable for light emitting diode and laser applications. Its electrical resistivity is as high as 10^{16} Ω cm which inhibits vertical current flow and makes it a very good insulator. However, due to this low conductivity of sapphire, the surface is highly expectable for surface charging which makes opto-electrical and electrical measurements, such as X-ray photoelectron spectroscopy (XPS) and scanning electron microscopy (SEM), very challenging. The thermal conductivity of sapphire at room temperature is only 46 $\mathrm{Wm^{-1}K^{-1}}$, which is much low lover than that of silicon (130 $\mathrm{Wm^{-1}K^{-1}}$) and 6H-SiC (490 $\mathrm{Wm^{-1}K^{-1}}$) [16] which might be a drawback for high power applications.

Heat treatment is commonly used prior to epitaxial growth in order to improve surface flatness and uniformity. The treatment is usually applied in hydrogen or oxygen ambient but treatments in air have also been shown to be successful [16]. Heat treatments have also shown to change the atomic structure of the surface and introducing superstructures of various kinds. As received sapphire (0001) substrate has a (1×1) surface structure both in air and in vacuum. Upon annealing this structure remains and the quality improves until temperatures around 900 °C is reached. At that temperature a weak $(\sqrt{3} \times \sqrt{3})R \pm 30°$ reconstruction is formed and upon further heating a $(\sqrt{31} \times \sqrt{31})R \pm 9°$ reconstruction will form which is stable to at least 1700 °C [17]. Figure 2.3 shows a reciprocal schematic representation (diffraction pattern) of these three types of surfaces. Both the $(\sqrt{3} \times \sqrt{3})R \pm 30°$ and $(\sqrt{31} \times \sqrt{31})R \pm 9°$ reconstructions are believed to be either oxygen deficient or aluminium rich where the aluminium cation, Al^{3+}, is reduced in the topmost layers [18, 19, 17]. Evidence of this is that the initial (1×1) structure can be regained

from $(\sqrt{31}\times\sqrt{31})R\pm9^\circ$ by heating it in oxygen ambient and the $(\sqrt{31}\times\sqrt{31})R\pm9^\circ$ reconstruction can be obtained by annealing (1×1) at around 800 °C in excess aluminium environment. In paper 1 of this thesis we compare the outcome of nitration of the (1×1) and $(\sqrt{31}\times\sqrt{31})R\pm9^\circ$ reconstructions using ammonia as nitrogen source.

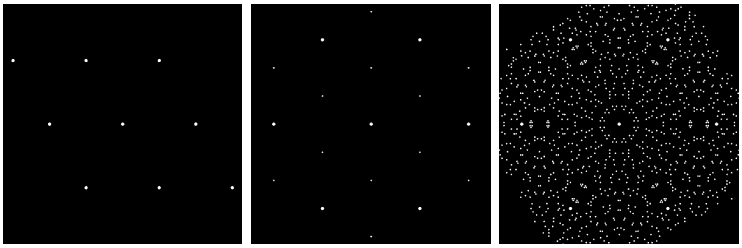

(a) (b) (c)

Figure 2.3. The three diffraction patterns due to different surface reconstruction of sapphire.

2.4 GaN on sapphire characteristics

There are three common crystal structures shared by the III-nitrides: the wurtzite, zinc blende and rocksalt structures. Under ambient conditions the wurtzite structure is the only one that is thermodynamically stable for bulk AlN, GaN and InN. The zinc blende phase can be epitaxialy grown as film on cubic surfaces such as Si, MgO and GaAs. The rocksalt structure can only be induced under very high pressures.

The wurtzite structure has a hexagonal unit cell with two lattice parameters a and c in ratio $c/a = \sqrt{8/3} = 1.633$. This structure is shown in figure 2.4 and is composed of two hexagonal close-packed (hcp) sublattices which are shifted with respect to each other along the three-fold c axis by the amount of $u = 3/8$ in fractional coordinates. Each sublattices are occupied by one atomic species only giving four atoms per unit cell. The symmetry of the wurtzite structure is given by space group $P6_3mc$ and the two inequivalent atom positions are $(\frac{1}{3},\frac{2}{3},0)$ and $(\frac{1}{3},\frac{2}{3},u)$. When the atom arrangement of the depositing layer is determined by the substrate crystal surface, one speaks of epitaxy-induced growth or just *epitaxy*, which results in some degree of lattice matching between the crystal-structure of the substrate and the depositing layer. In practice, the only fundamental criterion for epitaxy seems to be a moderately small fractional mismatch, f, in the atomic periodicity's

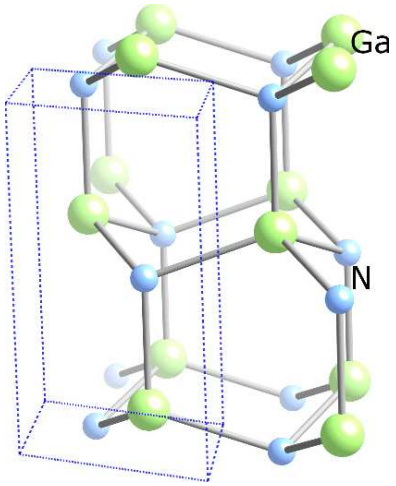

Figure 2.4. The wurtzite crystal structure of GaN. The dotted area represents the unit cell and different coloured circles represent the two different atom species.

of the two materials along the interface. One thus defines [20].

$$f = \frac{(a_e - a_s)}{(a_e + a_s)/2} \approx \frac{a_e - a_s}{a_s}$$

Where a_e and a_s represent the atomic spacing along some direction in the film crystal and the substrate interface, respectively. The crystallographic structures of the substrate and the film must match as well as possible in order to get well defined film growth. Generally, one needs $f < 0.1$ or so to obtain epitaxy, because for $f > 0.1$, few of the interfacial bonds align well enough [20]. Epitaxial growth eliminates grain boundaries, allows a good control of crystal orientation, provides a potential for atomically smooth growth and enables atomic scale structure definition.

Since bulk III-V nitride crystals are are not commercially available, wurtzite GaN films must be grown heteroepitaxilly on foreign substrates such as sapphire (0001) (Al_2O_3). Most research work has been carried out using either nitride compounds or buffer compound which acts as a catalyst for the formation of GaN. In our work we wanted to grow GaN films on sapphire substrate using pure nitrogen (N) and gallium (Ga) atoms as a deposition material using MBE. The advantage of sapphire for growing α-GaN is the hexagonal symmetry of the oxygen cation sub-lattice. The symmetry and atomic bonding are however quite different between the two materials (see figure 2.5) [21]. The main characteristic constants of GaN, AlN, InN and sapphire are listed in table 2.1.

Table 2.1. Characteristic properties of GaN, AlN and sapphire [22].

Material	c-lattice constant [nm]	a-lattice constant [nm]	c-thermal exp.coeff. [K^{-1}]	a-thermal exp.coeff. [K^{-1}]	a-lattice mismatch [%]
GaN	0.5185	0.3188	3.17×10^{-6}	5.59×10^{-6}	0
AlN	0.498	0.3111	5.3×10^{-6}	4.2×10^{-6}	2
InN	0.572	0.3542	3×10^{-6}	4×10^{-6}	-12
6H-SiC	1.511	0.308	4.68×10^{-6}	4.2×10^{-6}	2
Sapphire	1.229	0.4758	8.5×10^{-6}	7.5×10^{-6}	-14

High quality epitaxial layers require substrate materials which have lattice constants and thermal expansion coefficients closely matching those of the overlayers, but no such substrates are currently available for GaN and its alloys[16]. Sapphire, which is a stable compound at high temperatures ($\approx 1000^\circ$ C) in vacuum, is the most common substrate for epitaxy of the group III nitrides and is what was used when GaN was epitaxially grown for the first time. Sapphire is relatively cheap, its crystal structure is usually of good quality and it is transparent which can be very useful for measurements which uses for example infrared radiation. The calculated lattice mismatch between the basal GaN and the basal sapphire plane is in fact larger than 30% but since the small cell of Al atoms on the basal sapphire plane is oriented 30° away from the larger sapphire unit cell, the actual mismatch is around 14% (see figure 2.5). However, even though the lattice mismatch seem relatively

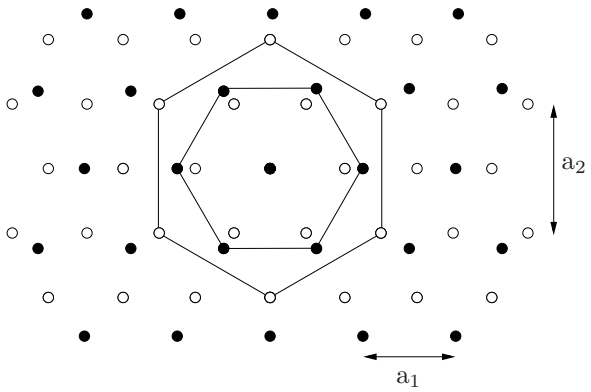

Figure 2.5. The epitaxial relationship between a sapphire substrate and GaN or AlN overlayer. The hexagons represent the unit cells of the two layers while the white dots represent the Ga atoms and the black dots the Al atoms.

small, it is still big enough to be the biggest obstacle in producing high quality single crystal III-nitrides. This is because upon cooling after growth, a thermal

strain is created between the two layers which causes thin films to crack or form polycrystalline compound. To overcome this lattice mismatch, a bufferlayer has to be introduced in order to easy the overlap between the two mismatching layers.

Chapter 3

Techniques

3.1 X-ray photoelectron spectroscopy

X-ray photoelectron spectroscopy (XPS) is a well established technique that utilises photoelectric effect to retrieve information about the chemical or elemental composition of the topmost layers of a surface under study. XPS is basically a chemical analyser, but with its extreme surface sensitive it can be utilised to extract all sorts of information from surfaces, including thin add-layer thickness and chemical environment of the atoms under study. In the most simple picture, a photon of known energy hits and kicks out a core electron on the sample surface. Such an electron is known as *photoelectron*. The energy of the photon has to be high enough to break the electron binding energy and also for the photoelectron to overcome the work-function of the solid. By measuring the energy distribution of the photoelectrons, the density of states of the solid can be obtained. If the energy is conserved, the overall process can be described according to:

$$E_{kin} = h\nu - E_{bin} - \Phi \tag{3.1}$$

where E_{kin} is the kinetic energy of the electrons, $h\nu$ is the photon energy, E_{bin} is the binding energy of the electrons and Φ is the work function of the solid. A schematic of this process can be seen in figure 3.1. Since each element has unique set of core levels, kinetic energies can be used to fingerprint elements, each element giving of a specific XP spectrum.

The surface sensitivity of the measurement depends on two things in particular; the *inelastic mean free path* of the excited electron and the angle, θ, under which it is detected. The distance, the electron is able to travel within the solid without loosing energy due to scattering with other electrons, is called the inelastic electron mean free path, λ. This distance depends in particular on the kinetic energy of the excited electron and as can be seen in figure 3.2, the XPS technique is most surface sensitive for electrons with kinetic energies around 20-100 eV. Figure 3.2

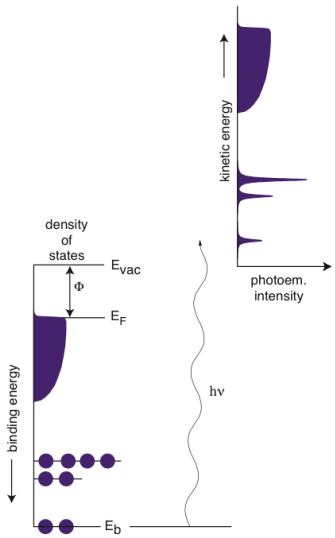

Figure 3.1. The energies involved in a typical photoelectron spectroscopy process. E_B is the binding energy of the photoelectrons, E_F is the Fermi energy of the surface, E_{vac} is the vacuum energy and Φ is the work function.

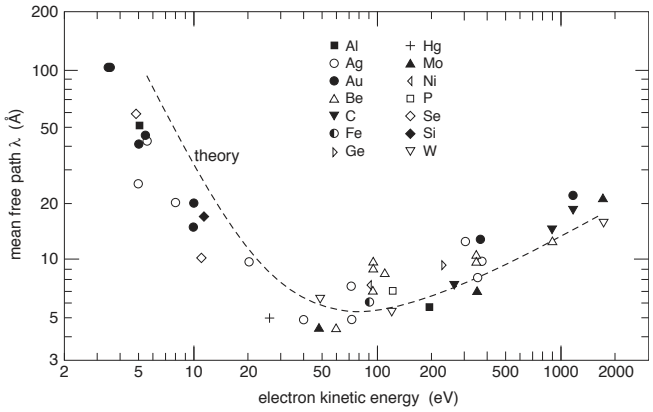

Figure 3.2. The electron mean free path of different elements as a function of their kinetic energy. The dots are measurements and the dashed curve is a calculation. Figure is taken Philip Hofmann personal homepage (from http://www.philiphofmann.net).

is know as the *universal electron scattering curve* and it describes the mean free paths of electrons for all materials within factor 2-3. The distance an electron can travel within a solid decays exponentially for distances greater than λ. This means that 95% of the signal intensity is derived from a distance $d' = 3\lambda$ inside the solid. Referring to figure 3.3 this corresponds to a vertical distance $d = 3\lambda\cos\theta$, hence giving the angular dependance of the signal intensity with respect to detection angle.

For a single crystal with no overlayer the signal intensity does not vary significantly with angle of detection, even though the vertical depth from which the electrons originate will not be the same. In the case when a thin overlayer, o, of thickness d is present on a substrate, s, the angular variation of signal intensity from a uniform thin overlayer is given by [23]:

$$I^o = I_0^o(1 - e^{-d'/\lambda}) = I_0^o(1 - e^{-d/\lambda\cos\theta}) \tag{3.2}$$

where I_0^d is the intensity from an infinitely thick overlayer, θ is the angle at which the emerging electron is measured under with respect to surface normal and d is the thickness of the overlayer (see figure 3.3). Equation 3.2 can not be used directly

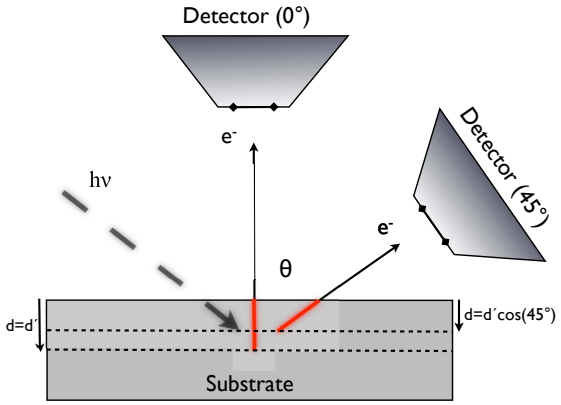

Figure 3.3. Surface sensitivity is strongly dependent on the take-off angle of the photoelectron. The red lines in the figure are equally long (d') but the vertical penetration depth (d) is different for the two setups.

to estimate the thickness of a add-layer since I_0^o is generally not know. However by watching the change in the signal from the underlying substrate, and fitting it to the following model [23]:

$$I^s = I_0^s e^{-d'/\lambda} = I_0^s e^{-d/\lambda\cos\theta} \tag{3.3}$$

one can achieve an estimation of the add-layer thickness since here I_0^s is the intensity from the substrate prior to deposition. This method is utilised in the paper [P1] to estimate the thickness of an AlN overlayer after nitration of sapphire with ammonia.

3.1.1 XPS Instrumentation

The instrumentation used for conventional XPS consists of a X-ray source and an analyser. The X-ray source is usually a twin anode source with both Mg Kα (1253.6 eV) and Al Kα (1486.3 eV) anodes both of which produce X-rays with high enough energy to excite deeply bound core electrons as well as loosely bound valence electrons. These X-rays have a relatively well defined energy with full width half maximum (FWHM) of $\Delta E_x = 0.7$ eV and $\Delta E_x = 0.85$ eV for Mg and Al respectively which makes them a good choice with respect to resolution (see equation 3.5). The most common type of electrostatic deflection-type analyzer used is called *concentric hemispherical analyser* (CHA) or spherical sector analyser. A schematic of such an analyser is given in figure 3.4. In the entrance tube of the

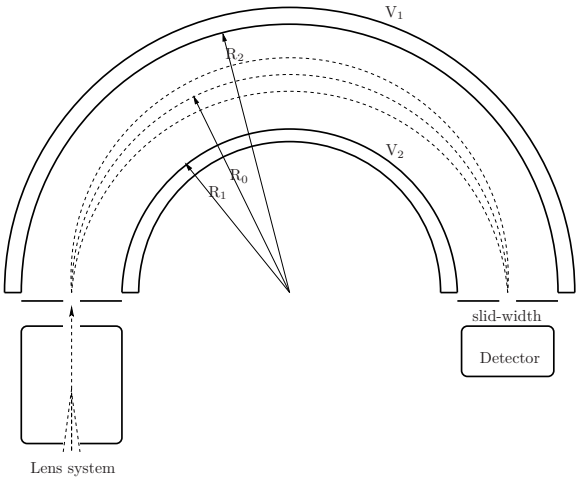

Figure 3.4. Path of photoelectrons in a concentric hemispherical analyser.

analyser the electrons are focused and retarded or accelerated to a predefined value called the *pass energy*, at which they travel through the hemispherical filter. A negative potential is applied on the two hemispheres, $V_2 < V_1$. The potential of mean path through analyzer is:

$$V_0 = \frac{V_1 R_1 + V_2 R_2}{2R_0} \tag{3.4}$$

An electron of kinetic energy equal to V_0 will travel in a circular path through hemispheres of radius R_0 and since R_0, R_1 and R_2 are fixed, in principle changing

V_1 and V_2 will allow scanning of electron kinetic energies following the mean path through the hemispheres. All the analysers used at MaxLab and at the lab in Kista were concentric hemispherical analysers.

There are number of factors that influence the energy resolution of a particular XPS signal but is mainly determined by three factors. The line width of the X-ray source, the line broadening due to the analyser and the natural line width of the particular core level under study. If each factor is expressed by a Gaussian function, then the total line width of a photoemission peak at half maximum (ΔE) can be expresses as:

$$(\Delta E)^2 = (\Delta E_x)^2 + (\Delta E_{an})^2 + (\Delta E_{nat})^2 \tag{3.5}$$

where ΔE_x is the line width of the X-ray source, ΔE_{an} is the line width due to the analyser and ΔE_{nat} is the natural line width. Sample dependent considerations are also important where localized charging may broaden lines regardless of the precision built into the instrument and therefore effective charge neutralization is an important part of any system.

The line width of the X-ray source (ΔE_x) is usually in the order of 1 eV but can be considerably reduced to around 0.3 eV with the use of a monochromator. A monochromator narrows the line width significantly and focuses the X-ray beam onto the sample. It also cuts out all unwanted X-ray satellites and background radiation reducing heat and secondary electrons to reach the sample. There are two main disadvantages associated with monochromated X-ray sources. First, the Bragg geometry requires the X-ray anode, quartz crystals and the sample under analysis to sit on a Rowland circle, so that the sample has to be carefully positioned at the focal plane of the monochromator. Second, specific action needs to be taken to correct the accumulation of charge at the surface of insulating samples. When a non-monochromated X-ray source is employed, the sample surface is exposed to low-energy electrons that originate from the aluminium foil window in the nose of the X-ray gun. This results in charge compensation that is essentially automatic and fairly uniform. A monochromated X-ray source, on the other hand, does not emit enough electrons to compensate for the departure of photoelectrons from an insulating surface. This is also the case for synchrotron generated X-rays as I found out when trying conduct measurements on the isolating Al_2O_3 substrate at MaxLab in Lund. At the lab in Kista, where twin anode source is used, the sample usually charged up a bit, but soon reached some kind of an equilibrium state where the charging became stable and constant resulting in a small charging shift of the core electrons peaks in the XP spectrum. However, at MaxLAB this equilibrium condition was never reached which meant that charging was constantly building up with time. So even though synchrotron generated light has many benefits one really has to evaluate each time whether it fits and improves the data of the undergoing study.

The natural line width (ΔE_{nat}) of the particular core level under study is determined by the Heisenberg's uncertainty relation; $\Delta E_{nat} \cdot \Delta t \approx \frac{h}{2\pi}$, where Δt is the life time of the core-ionized atom resulting in a line width of less than 0.1 eV. The main contribution to the overall resolution is the linewidth of the X-ray source but the only one of the three that is really controllable is the broadening due to the analyser, ΔE_{an}. The *relative resolution* power, R, of a particular photoelectron peak with kinetic energy E_{kin} and FWHM ΔE, is defined as:

$$R = \frac{\Delta E}{E_{kin}} \tag{3.6}$$

It is apparent from this equation that the resolution for each peak in the XPS spectrum is different depending on the kinetic energy of photoelectron in each case. In order to get a uniform resolution across the spectrum the easiest way is to retard the electrons entering the energy analyzer to fixed kinetic energy, which is the previously mentioned *pass energy* E_0, so that a fixed resolution applies across the entire spectrum. For a concentric hemispherical analyser the relative resolution is given by [23]:

$$\frac{\Delta E}{E_0} \approx \frac{s}{2R_0} \tag{3.7}$$

where s is the mean width of the slit in which the electrons enter the analyser (see figure 3.4). From equation 3.7 one sees that the increased R_0 and/or decreased E_0 results in an increase in relative resolution but lower E_0 also means fewer electrons reaching the detector. Hence there is a trade-off between high signal intensity, for high pass energy, and high resolution for low pass energy.

3.1.2 Synchrotron radiation

In addition to traditional X-ray sources as are used in conventional labs, X-rays can be generated more intensely and more effectively using synchrotron radiation sources. These generators are huge storage rings that keep electrons on a circular path at relativistic speeds using massive bending magnets. The energy of the electrons is usually in the GeV range. When an electron bends from a straight path it is actually experiencing centrifugal acceleration meaning that the electron will radiate according to Maxwell's equations. Due to the relativistic speed of the electrons the observed frequency of the light will be changed by the factor γ^2 because of Doppler effect and relativistic Lorentz contribution resulting in wide (Bremsstrahlung) observed frequency in the X-ray range. Another effect of relativity is that the radiation pattern is also distorted from the isotropic dipole pattern expected from non-relativistic theory into an extremely forward-pointing cone of radiation. This makes synchrotron radiation a very bright and well defined source of X-rays and ideally well suited for monochromatisation. The fact that the electrons are accelerated in the plan of the storage ring, makes the radiation linearly polarised when observed in that plane and circularly polarised when observed at

a small angle to that plane. These different polarisation can be of use for certain measurements techniques. The main advantage of synchrotron radiation is, as mentioned before, the high brightness and intensity, the high level of polarisation, the widely tuneable energy of the light from eV to MeV and last but not least the low cross section and small solid angle of emission which come into play in equation 3.5 (ΔE_x) and makes the resulting photoelectron peaks more resolvable than traditional X-ray sources are capable of. Synchrotron radiation at MaxLab was used for the measurements carried out in paper [P3].

3.1.3 XPS analysis

In XPS one measures the intensity of photoelectrons as a function of their kinetic energy. Photoelectron peaks are labelled according to the quantum numbers of the level from which they originate. An electron with orbital momentum l and spin s has a total angular momentum $j = l + s$ and since $s = \pm 1/2$, each level with $l \geq 1$ has two sublevels with an energy difference called the spin-orbit splitting. This is why many XPS peaks appear in pairs (doublets) with well defined intensity ratio and energy split. The exact location of the XPS peak depends on the chemical environment from which the electron originates (see figure 3.1). This fact can be very usefull in order to determine the local bonding or valence of the atom from which the electron originates and manifests itself in small shifts in the peak position, know as *chemical shifts*. Chemical shifts can be very small and hence it can be difficult to distinguish between peaks who lie close together. If one suspects that a XPS peak might be composed of more than one single peak it is feasible to try to extract more information by fitting the the peak using data-analysis software of some sort. The usual practice is to fit each peak using Voigt functions and monitor the change in both peak intensity and possition. In paper [P1] where we were studying the nitridation efficiency of low pressure ammonia on sapphire, we suspected the broad Al2p peak to be composed of two smaller peaks attributed to two different types of core electrons. One type originating from aluminium atoms in contact with oxygen in the sapphire and another type in contact with nitrogen in the thin nitrated layer. And indeed this turned out to be the case since the chemical shift and the intensity matched the accepted values for Al2p core electrons in Al_2O_3 and AlN

Before a XPS measurement can be started, certain parameters have to be set in such a way that the system is optimised on gathering the information needed each time. This includes choosing appropriate photon energies, X-ray slit widths, setting the detection angle and pass energies etc. In short, the following applies:

- The surface sensitivity of a measurement depends on the photon energy and detection angle.

- The photoelectron cross-section depends on the photon energy.

- The total photon flux and hence the intensity of the photoelectron signal depends on the photon energy and on the slits width.
- The linewidth of a the beam and hence the resolution depends on the photon energy, width of the X-ray slit and pass energy.
- If operating in binding-energy mode, the position of Auger peaks will depend on the photon energy, so the photon energy must be chosen in such a way that the Auger peaks do not coincide with interesting core electron peaks.

The photon energy is the single most important factor to consider before conducting XPS measurements. Surface sensitivity depends indirectly on the photon energy through the relation between the photon energy, the core electron binding energy and the resulting photoelectron kinetic energy in equation 3.1. The energy of the excitation photons must exceed the binding energy of the core electron to be detected, however not all incoming photons are able to excite a core electron even though they have the sufficient energy to do so. The photon efficiency, or the likelihood of producing a photoelectron, is known as the photoelectron *cross-section*. So the likelihood of the generating a photoelectron depends on the specific energy of the photons used for excitation.

Cross section is also important for quantitative analysis of spectra. Lets say an overview spectra is recorded at $h\nu = 500$ eV. On the spectrum there are two equally high peaks originating from some known materials under study. In order to get qualitative information about the ratio of these two materials in the surface, the intensity of respective peaks have to be divided with the specific cross-sectional value of each material for a given photon energy (see equation 3.8).

The photon flux depends on the energy selected. Usually the flux is measured as a function of photon energy for all slit-widths available. There may be a variation of factor $2 - 3$ between energies only 100 eV apart for photon energies above 100 eV, so for low signal measurements the choice of photon energy should be taken into serious consideration.

The size of the X-ray slit decides the amount of photon flux exposed to the sample. For sensitive samples, which can not handle substantial intensities, narrowing the slit-width is the easiest way of limiting the flux. The slit also affects the resolution of the measurements since it narrows the linewidth (FWHM) of the incoming beam. Usually one chooses large slits for alignment using zero-order light and for overview scans. The most common slit sizes are 190, 92, 44, 16 and 6 μm. Sizes 190 and 6 are rarely used.

The orientation between sample and the detector is important with respect to surface sensitivity. The vertical penetration depth goes as cosine of the angle between

the detector and the sample-surface normal as is emphasised in equation 3.2. The higher the angle, the greater surface sensitivity (see figure 3.3).

X-ray photons are also capable of creating *Auger electrons*, which are secondary electrons produced as a result of the core level photoelectron process. Unlike photoelectrons, Auger electrons kinetic energy is not determined by the energy of the incoming photon but by the energy separation of the two levels involved in the Auger process. The energy is thus fixed and may coincide with the kinetic energy of a photoelectron from a different element and thus affect the binding energy intensity spectra of that particular element. Photon energy used for a particular experiment must be chosen with this in mind.

A standard way of achieving energy reference is by measuring the Fermi level of the metallic sample holder close to the sample. Since two materials brought into contact align their Fermi levels, this must mean that the measured Fermi level of the sample holder is the same as that of the sample. Fermi levels should be measured for the same energies as are used for measuring core levels. Usually the Fermi level is put equal to zero and all recorded energies scaled with respect to that. Other reference methods include recording energies with respect to adventures (dirt) carbon on surfaces or to use second order light. The signal intensity

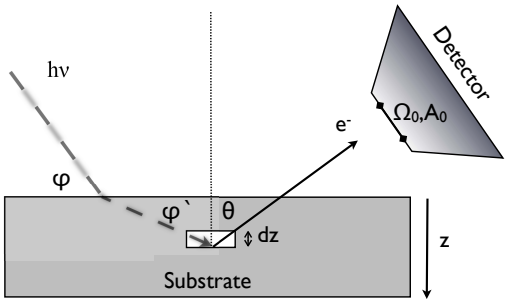

Figure 3.5. Signal intensity considerations

from photoelectrons depends on various factors. Assume a small volume segment of thickness dz within the substance being measured from which the photoelectrons originate. Only electrons emitted at an angle θ with respect to the normal will enter the analyzer and contribute to the spectrum. The intensity will depend on the following factors [24, 25, 26]:

1. Photon intensity (flux) according to:

$$\gamma(1-r)\frac{\sin(\phi)}{\sin(\phi')e^{\frac{-z}{\lambda_{h\nu}\sin(\phi')}}}$$

Where γ is the incident X-ray flux, r is the coefficient of reflection and $\lambda_{h\nu}$ is the attenuation length of X-ray photons. The reflection and refraction can be ignored for $\phi > 5°$. Generally the flux is not know and it is usually necessary to eliminate this factor by considering intensity ratios rather than absolute values.

2. The number of atoms in the volume element:

$$\frac{\rho A_0}{\cos(\theta)}dz \quad \text{or} \quad \frac{\rho A_0}{\sin(\phi)}dz$$

Where A_0 is the analyzers aperture size and ρ is the function describing the variation in the concentration of atoms with depth. This geometric factor can thankfully be eliminated by considering intensity ratios as before.

3. The probability of photoemission into the analyser:

$$\frac{d\sigma}{d\Omega}\Omega_0$$

Where σ is the photoemission cross-section and Ω is the angle between the photoelectron path and the analyzer-substrate axis. Ω_0 is a function of the lens program an aperture settings and usually not know, but can be avoided by using intensity ratios rather than absolute value.

4. The probability that a photoelectron will escape the sample without loosing energy:

$$\frac{-z}{e^{\lambda(E)\cos(\theta)}}$$

Where $\lambda(E)$ is the photoelectron kinetic energy and material-dependant inelastic mean free path described before. It is the attenuation of the flux of emerging photoelectrons that gives XPS its surface sensitivity.

5. The analyzer transmission function and detector efficiency:

$$D_0 F\left(\frac{E_0}{E}\right)$$

This function basically describes the efficiency with which the photoelectrons are transported through the analyzer to the detectors as a function of the analyzer energy. Usually information of this can be found within the software used to measure the signal intensity.

Ignoring the reflection and refraction of the incident X-rays and integrating the product of these five terms gives the intensity of the observed peak:

$$I_D = \gamma A_0 \Omega_0 D_0 F \left(\frac{E_0}{E}\right) \frac{d\sigma}{d\Omega} \frac{1}{\cos(\theta)} \int_0^D \rho(z) e^{\frac{-z}{\lambda(E)\cos(\theta)}} dz$$

Taking the peak intensity ratios cancels many parameters:

$$\frac{I_D^A}{I_D^B} = \frac{F^A \sigma^A \int_0^D \rho^A(z) e^{\frac{-z}{\lambda^A \cos(\theta)}} dz}{F^B \sigma^B \int_0^D \rho^B(z) e^{\frac{-z}{\lambda^B \cos(\theta)}} dz}$$

For homogeneous samples (ρ = constant), setting $z = D = \infty$ and integrating over the thickness of the sample, one ends up with:

$$\frac{I^A}{I^B} = \frac{F^A \sigma^A \rho^A \lambda^A}{F^B \sigma^B \rho^B \lambda^B}$$

So the sample composition can be expressed as the ratio of atomic concentration by correcting the observed peak intensity by the transmission function, the photoemission cross-section and the electron-mean-free-path according to:

$$\frac{\rho^A}{\rho^B} = \frac{F^B \sigma^B I^A \lambda^B}{F^A \sigma^A I^B \lambda^A}$$

For a simple quantitative analysis, λ can be assumed to be a simple function of the photoelectron kinetic energy ($\lambda \approx E_k^2$) (see figure 3.2 for electron mean free path) where, $0.5 < a < 1$. The factors $F\sigma\lambda$ are usually combined into a relative sensitivity factor, S which can be found in various photoelectron spectroscopy tables and on the world wide web. The main factor in S is the atomic cross section so in some cases, to get a rough estimation on the ratio, the sensitivity factor is replaced by the atom-cross-section, σ.

$$\frac{\rho^A}{\rho^B} = \frac{I^A/S^A}{I^B/S^B} \approx \frac{I^A/\sigma^A}{I^B/\sigma^B}$$

The ratio:

$$\frac{\rho^A}{\rho^A + \rho^B}$$

is nothing else than the molar fraction content X_A of the element A for a two-element system. A generalized expression for determination of the atomic fraction of any constituent in a sample can thus be written as:

$$X_A = \frac{I^A/S^A}{\sum_i I^i/S^i} \tag{3.8}$$

Where the summation is over all the constituents of the surface. The tabulated value of S depends on whether the intensity I is measured as a peak area or as a peak height. Equation 3.8 was used in papers [P1] and [P3] in order to estimate the relative concentrations of various elements on the sapphire surface and GaN surfaces respectively.

3.2 Low electron energy diffraction

Techniques that rely on some sort of scattering from surfaces are an important source of information in surface research. Scattering can be anything from a surface being exposed to light to heavy particle bombardment. Information can be extracted from studying the elastic part the interaction as well as the inelastic part, all depending on what kind of information one is looking to obtain. In order to study the geometry and symmetry of crystalline surfaces one needs a scatterer that does not penetrate too deep into the solid. This means that we are looking for a scatterer with a de Broglie wavelength, $\lambda = h/p$, of the same magnitude as typical distances in the crystal (orders of Angstroms). In this case a useful diffraction phenomena can be expected and also surface sensitive of the technique is guaranteed. *Low electron energy diffraction* (LEED) is a scattering process that fulfils both these criteria. It relies on low energy electrons, with short mean free paths, to obtain information about crystallographic quality of a surface or topmost layer by studying the elastic part of back-scattered electrons. As mentioned in the introduction, it is important to have a well ordered or at least well defined surface in the beginning of an experiment and it is also important to be able to monitor any geometrical change taking place during an experiment. This makes LEED a powerful and essential tool in any solid-state surface labs today.

In LEED, a beam of low energy electrons are accelerated to energies ranging from 50 to 300 eV and incident on a crystalline surface. The elastically back-scattered electrons interact to give rise to diffraction spots that appear on a phosphorous screen located a certain distance away from the sample. A typical LEED setup can be seen in figure 3.6. It consists of a basic electron gun producing monochromatic electrons and a detector system which detects only the elastically scattered electrons. The detector system consists of a set of grids and a fluorescence screen. The grids are kept at different potentials, which filter away inelastically scattered electrons. The elastically scattered electrons, that are allowed to pass, hit the fluorescence screen which illuminates if constructive interference takes place at that specific point. Behind the screen there is a window in the vacuum system so that the LEED pattern can be observed directly or recorded with a camera.

LEED, as well as other kinds of particle-surface scattering processes, can essentially be described by the *kinematic theory*. From kinematic theory, the surface unit cell size and symmetry can be determined. The condition for constructive in-

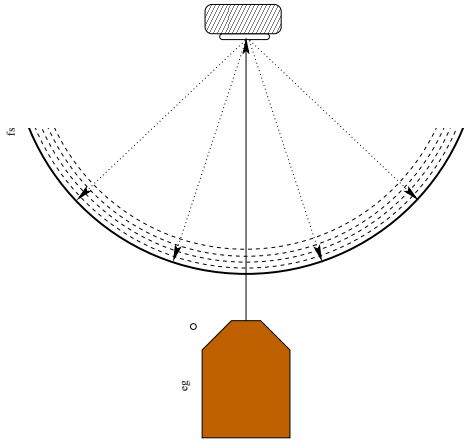

Figure 3.6. Schematic of a typical LEED setup. Low energy electrons are accelerated toward the sample surface were they are backscattered toward a fluorescence screen where interference pattern appears. Unwanted inelastically scattered electrons are filtered out by retarding screens.

terference of elastically scattered electrons is given by *Bragg's diffraction condition* which states that the scattering vector component parallel to the surface ($\mathbf{K}_{||}$) must be equal to the two dimensional surface reciprocal lattice vector $\mathbf{G}_{||}$. This can be described mathematically as:

$$\mathbf{K}_{||} = \mathbf{k}'_{||} - \mathbf{k}_{||} = \mathbf{G}_{||} \tag{3.9}$$

$$\mathbf{K}_{||} = h\mathbf{g_1} + k\mathbf{g_2} \tag{3.10}$$

where $\mathbf{k}_{||}$ and $\mathbf{k}'_{||}$ are the incident and final electron wave vectors respectively and h and k are arbitrary integers. Bragg's condition in this form is know as *Laue condition*. As can be noticed, then the vertical component, $\mathbf{k}_{\perp}$, does not come into play here. This is because for a two dimensional lattice, $\mathbf{k}_{\perp}$ is in fact infinite in real space and hence in reciprocal space the points it is represented by are infinitely close together and thus form some sort of rods. However the conservation of energy forces a restriction on the vertical component by demanding that for elastic scattering the total energy prior to scattering and after is conserved:

$$|\mathbf{k}| = |\mathbf{k}'| \tag{3.11}$$

The observed LEED pattern is a two-dimensional reciprocal lattice of the ordered surface projected onto a two-dimensional real plane. The position of the LEED spots can be determined using *Ewald construction* (see figure 3.7). By drawing the appropriate vectors by applying the constrictions from equations 3.10 and 3.11, as shown in figure 3.7, one can determine exactly where to expect the scattering

condition to be fulfilled according to equation 3.10. The condition is fulfilled for every point at which the sphere crosses a reciprocal lattice rod. The diffraction

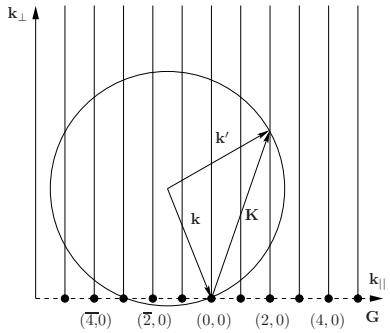

Figure 3.7. Ewald construction for elastic scattering on a two dimensional surface.

pattern represents the symmetry of the surface and in fact, for such a system the diffraction pattern will be an image of the surface reciprocal lattice. Also, the resulting diffraction maxima can be directly associated with the reciprocal lattice giving information about interatomic distances. In my work LEED pattern is used to study the surface symmetry before, during and after various treatments of the surface ([P1] and [P3]).

3.3 High resolution X-ray diffraction

High resolution X-ray diffraction (XRD) is a widely used technique to obtain information of bulk-crystal quality and structure. Just like LEED, XRD relies on scattering but unlike LEED where of electrons are scattered elastically from a surface atoms, XRD relies on X-rays which scatter elastically from the electrons in the crystal. As mentioned in the LEED section, typical interatomic distances in solids are on the order of an Angsrom. An electromagnetic probe of the microscopic structure of a solid must therefore have a wavelength at least this short. According to $E = h\omega = \frac{hc}{\lambda}$, energies in the range 10×10^3 eV are needed to produce such short wavelengths which is exactly the energy characteristic of X-rays. X-rays can travel deep into the bulk of the material under study and since the electron density has the periodicity of the crystal, the superposition of the scattered waves produces a diffraction pattern that is related to the periodicity of the crystal. The X-ray beam is incident under a certain angle, θ with respect to the sample and a detector or placed under the same angle on the opposite side (see figure 3.8). The diffraction intensity is then measured by scanning over different incident and diffraction angles. The atoms in a crystal form different parallel planes each of which correspond to a point in the Fourier space. Thus, each plane gets a point coordinate in three-dimensional Fourier space which are the *Miller* indices $(h, k.l)$ of the plane. When

incident waves hit the electrons of atoms in a certain plane they diffract and since the detector is placed under the same angle as the wave of incident, a constructive interference occurs at the detector site and a signal is picked up as an intensity peak (Bragg peak). By varying the angle, θ, each plane of atoms in the crystal lattice is probed giving information about lattice constant and crystal structure.

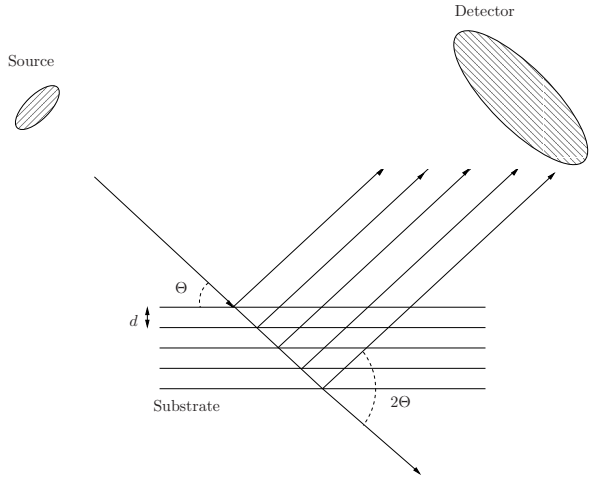

Figure 3.8. X-ray diffraction from a substrate. The rays are diffracted from lattice planes separated by a distance d

.

The previously mentioned Laue approach can be used to explain the condition for a constructive interference in XRD but a more widely used way of viewing the scattering of X-rays by a perfect periodic structure is by using *Bragg* formulation which is probably best know in optics to describe light scattering from periodic structures, such as gratings. In Bragg's formalism a certain set of parallel crystal planes $(h, k.l)$ are considered to be distance d_{hkl} apart. The conditions for a sharp peak in the scattered intensity are: that the X-rays should be specularly reflected (incoming angle equal to exit angle) and that the reflected rays from the successive planes should interfere constructively. The path difference between two specularly rays reflected from adjoining planes is $2d_{hkl} \sin\theta$. This path difference must be an integral number of the X-ray wavelength.

This leads to the Bragg condition for constructive interference:

$$n\lambda = 2d_{hkl}\sin\theta \tag{3.12}$$

In general the spacing between adjacent lattice planes perpendicular to $\mathbf{K}$ is given by equation 2.6, which means that the relationship between the plane distance d_{hkl} in cubic crystals ($a = b = c$) and the distance between the atoms a is simply given by:

$$d_{hkl} = \frac{a}{\sqrt{h^2 + k^2 + l^2}} \tag{3.13}$$

XRD is thus a powerful technique to determine the crystallographic structure of solids. In paper [P2] XRD is used to monitor changes in inter-atomic distance of sapphire substrates after various temperatures treatments.

3.4 Reflection high energy electron diffraction

Reflection high-energy electron diffraction (RHEED) is a powerful technique for studying surface structures of flat surfaces as well as surface phase transitions. It is sensitive to surface changes, either due to structural changes or due to adsorption and is in principle simple, requiring only an electron gun, a phosphor screen and a clean surface. A schematic of the experimental setup for RHEED can be seen in figure 3.9(a). Since the sample surface is monitored under a glancing angle the sample surface is not in any way affected by the setup. This makes RHEED ideal as an *in situ* probe to monitor growth of thin films both in research and in industry. The drawback of RHHED is that its interpretation is complicated due to unusually asymmetric scattering geometry and due to multiple scattering processes [27].

Despite the popularity of RHEED, there is no complete formal theory for it, unlike the case for LEED. However number of simplified kinematical approaches have been introduced that are useful for understanding the basic idea of RHEED. These include the simple *geometric theory*, the elaborated *dynamical theory* and the sufficiently accurate *kinematic theory*. The kinematic theory of RHEED diffraction pattern is in fact nothing else than the well known kinematic theory of X-ray diffraction pattern. The main difference between the two is that in the former we use high electron beams to analyse a two dimensional surface while in the latter we use X-rays to analyze a three dimensional crystal. However, because of electron-atom interaction, the penetration depth of RHHED is extremely small meaning that it is primarily sensitive to the atomic structure of the first few planes of the crystal lattice. In kinematic theory, one assumes that the electrons are all scattered elastically from the surface and that only the incident beam produces diffracted beams. Both XRD and RHHED can be partly explained by the approach of kinematic theory which is applicable to all kinds of particle-surface scattering, elastic and inelastic. The theory can however not describe the details of the intensity distribution in low-energy electron scattering[13]. To obtain information about that, dynamical

RHEED theory is necessary since it allows for mulitple scattering envents at the surface in addition to inelastic scattering. Elastic scattering can tell us something about the symmetry and the geometric arrangements of atoms near the surface, whereas inelastic scattering processes, where energy quanta are transferred to or from the topmost atomic layers of a solid, yield information about possible excitations of the surface or interface.

The kinematic theory of diffraction can be explained by various methods including *Bragg condition of reflection*, *Laue formalism* or by the help of the graphical method of *Ewald spheres* as has been previously done in the LEED and XRD section of this thesis. All of these methods of explanation are based on Fourier analyzes of the periodicity of the crystal structures. These conditions allow you to predict the locations of the diffraction maxima but not their relative intensities. Each combination of incident ($\mathbf{k}$) and diffracted ($\mathbf{k}'$) wave vectors probes a certain plane in the crystal lattice and corresponds to a point in the Fourier space for electron density waves. In case of RHEED pattern analyses, only two dimensional space is required. The reciprocal lattice in two dimensions is defined in the following way:

$$\mathbf{G} = h\mathbf{b}_1 + k\mathbf{b}_2 \tag{3.14}$$

where $\mathbf{b}_1$ and $\mathbf{b}_2$ are the reciprocal basis vectors defined in equation 2.4. In RHEED and LEED it is the intensity of the scattered waves that gives the desired information.

$$I(\mathbf{K}) \propto \left| \sum_{\mathbf{G}} \int e^{i(\mathbf{G}-\mathbf{K})\cdot\mathbf{r}} \right|^2 \tag{3.15}$$

where $\mathbf{K} = \mathbf{k}' - \mathbf{k}$. The integral in the above equation has its maximum when the previously mentioned Laue condidtion is fulfilled ($\mathbf{K} = \mathbf{G}$). Scattering from lattices thus leads to diffracted beams that give constructive interference when the difference between the incident and scattered waves is equal to a reciprocal lattice vector $\mathbf{G}$. Just as with low energy electron diffraction one can represent this condition pictorially by means of Ewald construction (see figure 3.9(b)). The two dimensional surface is visualized in the reciprocal space as a net with rods extending infinitely in the direction perpendicular to the surface. The Laue condition is then fulfilled for every point at which the sphere crosses a reciprocal lattice rod. These considerations are exact only in the limit of scattering from a true two dimensional network of atoms.

In a real RHEED experiment, however, the primary electrons penetrate several atomic layers into the solid meaning that the diffraction pattern will originate from several of the top-most layers of the material. This has the consequence that the third reciprocal vector in the Laue condition comes into play. Because of the extremely high energy of the incoming electrons the diameter of the Ewald sphere will be much larger than a typical lattice vector. The reciprocal lattice rods shown

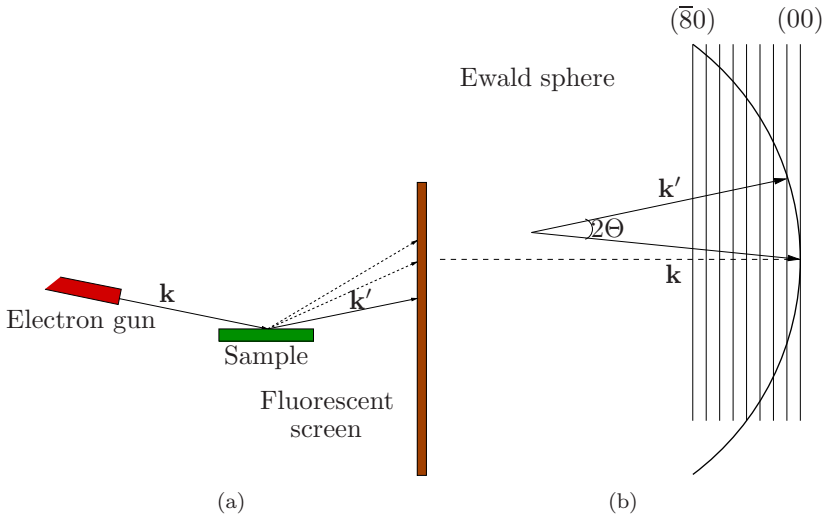

Figure 3.9. (a) Schematic of the experimental setup for RHEED. High energy electrons are accelerated towards the sample surface (**k**) and forward elastically-scattered electrons (**k′**) interfere at the fluorescent screen. (b) The Ewald sphere construction for RHEED. **k′** and **k** are scattered and primary wavevectors respectively. The sphere radius $|\mathbf{k}'| = |\mathbf{k}|$ is much larger than the distance between the reciprocal lattice rods (hk).

in figure 3.9(b) are also cut at a grazing angles in the region corresponding to a diffracted beam emerging close to the surface. The Ewald sphere "touches" the rods of the reciprocal lattice. Both the sphere and the reciprocal lattice rods are smeared out to some extent, due to the angular and energy spread of the primary beam, respectively, and due to the deviations from ideal translational symmetry in the surface[13] [27]. This results in a diffraction pattern consisting not of spots but rather streaks corresponding to the sections of the reciprocal lattice rod intersected (see figure 3.10(b) and 3.10(c)). If the surface is extremely flat and ideal and if the instruments in use are of high quality one can occasionally observe very sharp diffraction spots[27].

3.4.1 RHEED pattern interpretation

In RHEED the incident electron strikes the surface of the sample at a very low angle and due to strong interaction of the electron beam and the electronic system of the sample, the penetration depth is limited to a few Angstroms [27]. Thus the electron can be considered to be diffracted by the 2-dimensional periodic structure of the topmost layer of the surface, a plane rather than a 3-dimensional periodic structure, a Bravais surface or net.

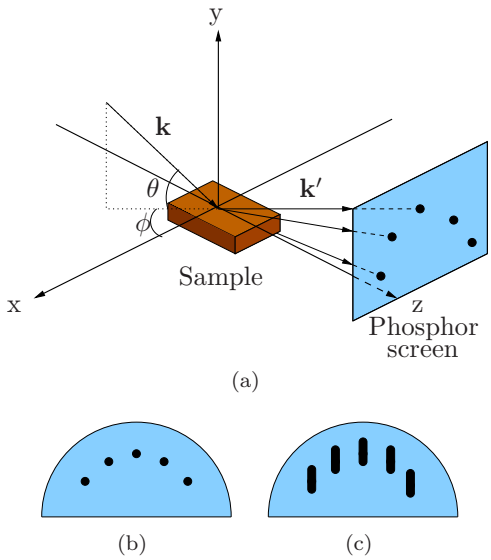

Figure 3.10. (a) An illustration of the fundamentals of RHEED. (b) Diffraction pattern from ideal smooth surface. (c) Diffraction from real smooth surface.

Figure 3.11 shows a diagram of the Ewald sphere intersecting a series of lattice rods lying perpendicular to the plane of the sample. This figure is the same as figure 3.9(b) but seen from the top rather than the side. In a continuous sample the rods become points in three dimensional space. x is the distance between the streaks seen on the phosphor screen and g is the distance in reciprocal space. The figure also shows that where the Laue diffraction criteria are met the Ewald sphere of the incoming electron waves will intersect the reciprocal lattice rods of the surface of the sample. This will result in streaks of spacing x on the phosphor screen. As the radius of the Ewald sphere is about two orders of magnitude greater than the modulus of the reciprocal lattice vector, we find that the angle between points intersecting the sphere, α, will almost be the same, or[27]:

$$tan(\alpha) = \frac{x}{L} \approx \frac{g}{k} = \alpha \tag{3.16}$$

Where g is the reciprocal space separation between atoms and L is the length from the sample to the phosphor screen. The energy of the electrons is given by[13]:

$$E = \frac{\hbar^2 k^2}{2m} \tag{3.17}$$

Where k is the numerical value of the wave vector ($k = \frac{2\pi}{\lambda}$), $\hbar$ is the Planck's constant and m is the mass of the electron. Since we know both the mass and the

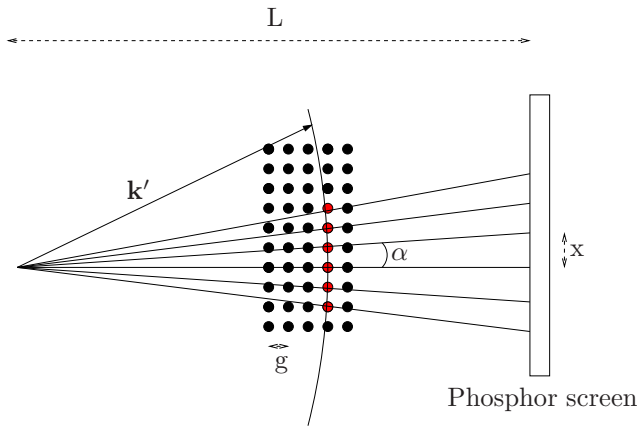

Figure 3.11. A diagram showing the Ewald sphere intersecting the series of lattice rods lying perpendicular to the plane of the sample. X is the distance between the streaks seen on the phosphor screen, L is the distance between the screen and the sample, g is the reciprocal space distance between the rods, α is the angle between the the points and $\mathbf{k}'$ is the wave-vector of the scattered beam

energy of the electrons (1-15keV) this quantity is completely pre-determined.

$$\lambda = \frac{h}{\sqrt{2mE}} \tag{3.18}$$

Using Laue condition (equation 3.10) we get that:

$$g = \frac{2\pi}{a} \tag{3.19}$$

Where a is the real space distance between the equivalent row of atoms parallel to the incident beam and g is the reciprocal distance between the atoms. Hence we get that:

$$a = \frac{L\lambda}{x} \tag{3.20}$$

The angle of incident can be determined from the radius of the zeroth Laue zone (the inner-most half circle visible on the phosphor screen), when the primary beam is directed along the principle axis of azimuth of the surface. The zeroth Laue zone contains the specular beam and hence its radius, which is independent of the incident energy, must be equal to $L\,tan(\theta)$, where θ is the glancing angle of incidence (see figure 3.10(a)) and L is the distance between the sample and the phosphor screen. If L is not known then it can be determined from the azimuthal separation of two diffracted beams, In this case the length is given by $\lambda a D_1$, where λ is given by equation 3.18, D_1 is the distance from the screen between two beams parallel to the surface and a is the separation between rows that are parallel to the incident

beam. If the radius of the first Laue zone is D_0 then the incident angle is given by $\theta = D_0/(\lambda a D_1)$.

In short, RHEED can help to:

- monitor surface morphology (surface flatness and domain sizes.)
- to recognise surface superstructures by analysing the arrangements of reflection spots/streaks in the patterns.
- for real time monitoring of atomic-layer growth by detecting the intensity oscillations in the specular reflections (growth rate monitoring).
- obtain information about lattice types and constants.

3.5 Atomic force microscopy

Atomic force microscope (AFM) is a high resolution scanning probe microscope technique, with demonstrated resolution of fractions of a nanometer, more than 1000 times better than the optical diffraction limit ($\lambda/2$). It is one of the foremost tools for imaging, measuring and manipulating matter at the nanoscale. The term "microscope" in the name is actually a misnomer because it implies that the surface is being looked at, while in fact the information is gathered by feeling or touching out the surface.

AFM has many advantages over other microscopic techniques. Since the AFM tip is actually in some sence feeling the sample surface, it is providing a true three dimensinal surface profile. This is very different from many other popular microscopic techniques such as optical microscopy and scanning electron microscopy (SEM), which only provide a two dimensional projection of the surface. Samples may also be scanned with AFM without special treatments and AFM is to some degree unaffected by sample charging and since the tip is actually never in direct contact with the sample, the surface under study is never damaged in any way when being scanned. Additionally, ex-citu AFM, does not require vacuum of any kind and can be used to study any thing from thin and thick film coatings, ceramics, composites, glasses, synthetic and biological membranes, metals, polymers, and semiconductors to living organisms. AFM used in ultra high vacuum have shown to give atomic resolution and its resolution is comparable with the resolution of scanning tunneling microscopy (STM) and transmission electron microscopy (TEM).

The main disadvantages of AFM compared to other techniques is the small image size it provides, the long scanning time and the hysteresis of the piezoelectric material and thermal drift. It is also somewhat complicated in operation, especially compared to its counterpart, the scanning tunnelling microscopy (STM). The tip itself is also extremely fragile and the slightest touch will defininitly damage it and

probably destroy it. However, with patience and experience most of these problems can be overcome which makes AFM the technique of choice for most scientists to study of phenomena such as abrasion, adhesion, cleaning, corrosion, etching, friction, lubrication, plating, polishing, surface structure and morphology.

3.5.1 AFM principle

When a sharp tip, usually made of silicon or silicon nitride, is brought within a short distance from a surface, the tip experiences two major forces: the static electric repulsive force between the ion cores and the static electric attractive force between the valence electrons and ion cores. This can be described by the van der Waals curve shown in figure 3.12. As the atoms of the tip and the surface are gradually brought together, they weakly attract each other. This attraction increases until the atoms are so close together that their electron clouds overlap and the atoms start to repel each other. When the total van der Waals force becomes positive(repulsive), the tip and the surface are in contact. In addition to the attractive and repulsive forces already mentioned, there often exists a capillary force exerted by a thin water layer often present in an ambient environment.

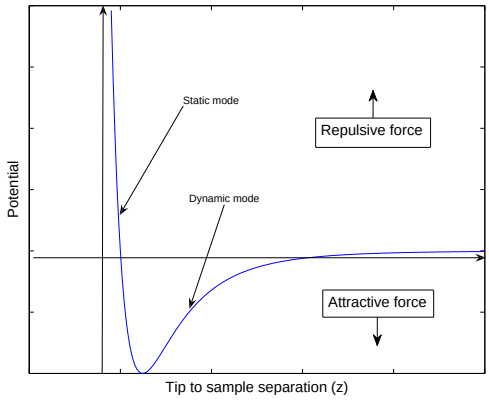

Figure 3.12. The van der Waals potential experienced by the AFM tip upon movement towards the sample. First, the tip experiences an attractive force, pulling the tip down toward the surface (non-contact region), but upon contact, the tip experiences a repulsive force from the surface (contact region).

An AFM is usually operated in either *dynamic mode* or *static mode*, sometimes referred to as non-contact and contact mode respectively. Figure 3.13 shows a schematic of the two modes. Dynamic mode can either be run in frequency modulated (non-contact) or amplitude modulated (tapping). In dynamic mode the can-

tilever, on which the tip is attached, is vibrated close to the surface of the sample. The total force between the tip and the surface is very low, which makes dynamic mode ideal for studying soft or elastic samples. Since the vibrating tip experiences very little lateral force, the lateral resolution is higher in this mode compered to static mode AFM. However, because the tip experiences extremely low force, this mode requires very sophisticated feedback control and in some cases some sort of sample preparation. In dynamic mode the cantilever is mechanically vibrated close

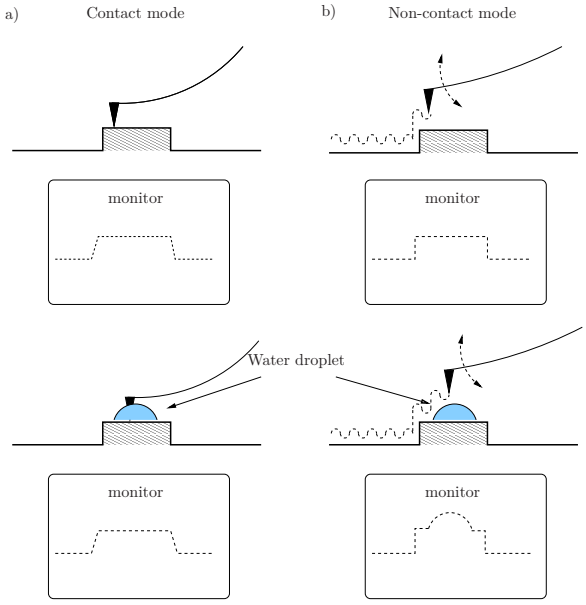

Figure 3.13. Concept diagram of AFM in static mode a) and dynamic mode b) scans on surfaces with and without water droplet.

to its resonance frequency (f_0), but at this frequency the amplitude of oscillation is close to the maximum. When brought close to the surface, the probe tip experiences an attractive force according to the van der Waal's potential shown in figure 3.12. Because of this, the cantilever vibration frequency will shift and with it the amplitude of oscillation as well. Mathematically this can be described as an effective change in the in spring constant of the tip from is intrinsic spring constant (k_0). This is new spring constant is called the effective spring constant (k_{eff}) and the following holds:

$$k_{eff} = k_0 - \frac{\delta}{\delta z} F \tag{3.21}$$

Where F is the force that the tip feels. The closer the tip gets to the surface, the higher the attractive force and the smaller k_{eff} becomes. The relationship between

the frequency and spring constant is given by:

$$f_{eff} = \sqrt{\frac{k_{eff}}{m}} \tag{3.22}$$

Where m is the mass of the cantilever. In dynamic mode AFM, one can either track the change in frequency of the oscillation (non-contact) or in amplitude (tapping mode). Both changes are usually detected using optical instruments. A laser spot is reflected from the top of the cantilever into an position-sensitive array of photodiodes. As the cantilever bends, the position of the laser beam on the detector shifts. Using a feedback loop this shift in amplitude or frequency can be compensated by changing the distance between the tip and the surface. By maintaining a constant cantilever amplitude and distance, dynamic mode AFM can measure the topography of samples surface by using feedback mechanism to control the vertical canner movement following the measurement of the force gradient represented in equation 3.21 and by that measure sub-angstrom vertical movement of the cantilever tip. The operation of dynamic mode can be quite difficult in ambient conditions because of existing thin layer of water on the tip and surface which causes problems in the engagement and retraction of the tip. As the tip is brought close to the surface, a small capillary bridge between the tip and the sample can form causing the tip to jump to contact. When looking for small vertical features where a water film is present on the sample, it would be more feasible to apply static mode AFM

In static mode one utilises the electrostatic repulsive part of the van der Waal's curve in figure 3.12 where the tip is experiencing a negative force from the surface. In this mode the cantilever is not vibrating but is pressed down with a certain force causing it to bend to accommodate changes in topography (see figure 3.13a). The sensitivity and resolution greatly depends on the sharpness of the tip and the sharper the tip the better. However if the tip is too sharp it is more likely to break or ware off over time. It is also important for the resonance frequency of the cantilever to be high so that it is as insensitive to external vibrations as possible. However, one also wants the force constant to be low in order to increase the sensitivity of the scan. Referring to equation 3.21, one sees that there is a trade-off between high frequency and low force constant, but by minimising the mass it is possible to optimise these parameters. The scanner gently traces the tip across the sample and the cantilever bending is picked up using the same optical technique as for the dynamic mode AFM. One of the drawbacks using static mode is that large lateral forces can be exerted on the sample as the tip is dragged over it. This can result in deformed images and damaged surfaces. Also absolute-force measurements tend to be noisy.

The choice for which AFM mode to use should be based on the surface characteristics of the material to be studied, such as stiffness, stickiness, feature sizes etc. Usually dynamic mode AFM offers less noise than static mode however it requires much more sophisticated instrumentation [28]. For the measurements done in the

appended article [P2], contact mode was used since the sapphire substrate under study is extremely stiff with very small vertical surface features that would be hard to distinguish through the thin water film using dynamic AFM.

3.6 Principle of spectroscopic ellipsometry

Spectroscopic ellipsometry (SE) is a non-perturbing optical technique that allows one to measure very accurately and with high reproducibility the dielectric properties such as complex dielectric function $\epsilon = \epsilon_1 + i\epsilon_2$ of a given material. It has numerous applications in different fields ranging from biology to semiconductor industry. The technique utilises the change that polarised light experiences upon reflection from surfaces, interfaces and thin films. A collimated beam of monochromatic light with know polarisation is incident on a sample surface and the polarisation of the reflected beam is analysed. Usually the incident light is circularly polarised and if the surface induces changes in either the transverse magnetic (TM) or transverse electric (TE) component of the light then the resulting reflected light will be elliptically polarised. The same is also true if the incident beam is linearly polarised. The degree of change depends only on the surface characteristics and incident wavelength and not on the absolute intensity or absolute phase.

A schematic of a simple ellipsometry setup can be seen in figure 3.14. Here a

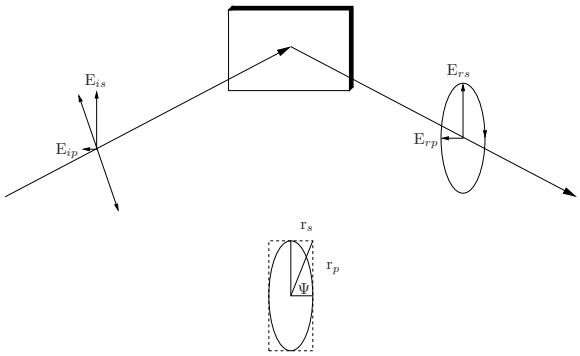

Figure 3.14. Basic schematic of the ellipsometry principle.

linearly polarised light is incident on the sample at known arbitrary angle and the reflected light becomes elliptically polarised. For arbitrary input light with phasor electric field components E_{ip} and E_{is}, the reflected light is given by:

$$E_{rp} = r_p E_{ip} \qquad E_{rs} = r_s E_{is} \tag{3.23}$$

Where r_s and r_p are the complex refraction coefficients. Taking the ratio of the respective sides of this equation one ends up with:

$$\rho = \frac{r_p}{r_s} \tag{3.24}$$

where ρ is dependent on the angle of incidence, wavelength and layer thickness and r_p and r_s can be determined from Fresnel's equations. It has become customary in ellipsometry to express ρ in polar form in terms of two ellipsometric angles Ψ and Δ as follows:

$$\rho = \tan(\Psi)\exp(i\Delta) \tag{3.25}$$

Δ is the phase shift between the two perpendicular components contributing to the ellipsoid and Ψ represents the relative amplitude ($\tan(\Psi) = |R_p||R_s|$). From these parameters various properties such as film thickness, refractive index, surface roughness, interfacial regions, crystallinity and anisotropy can be deduced using an appropriate optical model. In the appended paper [P2] we use ellipsometry to determine crystallographic structure changes and surface morphology of sapphire after various annealing treatments.

Chapter 4

Results

Here follows a summary of the results from the appended papers and manuscript. More detailed results and discussions can be found in the papers and the manuscript themselves.

4.1 Paper [P1]

As was discussed in chapter 1 the relatively large lattice mismatch between the sapphire substrate and the GaN epilayer poses a problem for achieving a good interface and high GaN crystal quality. One way of overcoming this problem is by introducing a AlN buffer layer in between the substrate and the GaN epilayer. The most common way of doing this is by means of surface nitration, either by plasma assisted nitrogen incorporation or by using ammonia. However, even though theses methods are widely used and becoming more and more standardised, the actual mechanism of the nitration process itself is yet to be fully understood. In paper 2 the effect of surface reconstruction and temperature on nitration efficency was investigated using LEED and XPS.

As-received sapphire (0001) substrate is unreconstructed but is known to transform to $(\sqrt{31} \times \sqrt{31})R \pm 9^\circ$ reconstruction upon thermal heating (see figures 4.1(a) and 4.1(b)). Our finding suggest that upon low pressure ammonia nitration the oxygen atoms on the surface are effectively exchanged by a nitrogen atom resulting in a AlN layer formation (see figure 4.1(c)). Our results also show that nitrogen is more efficiently incorporated on the reconstructed surface than on a unreconstructed one. In fact we were unable to nitrate an unreconstructed surface using low pressure ammonia. The optimum nitration temperature for reconstructed surface where, adsorption, desorption and thermal cracking of the ammonia were at optimum, was found to lie somewhere around 850 °C (see figure 4.1(d)).

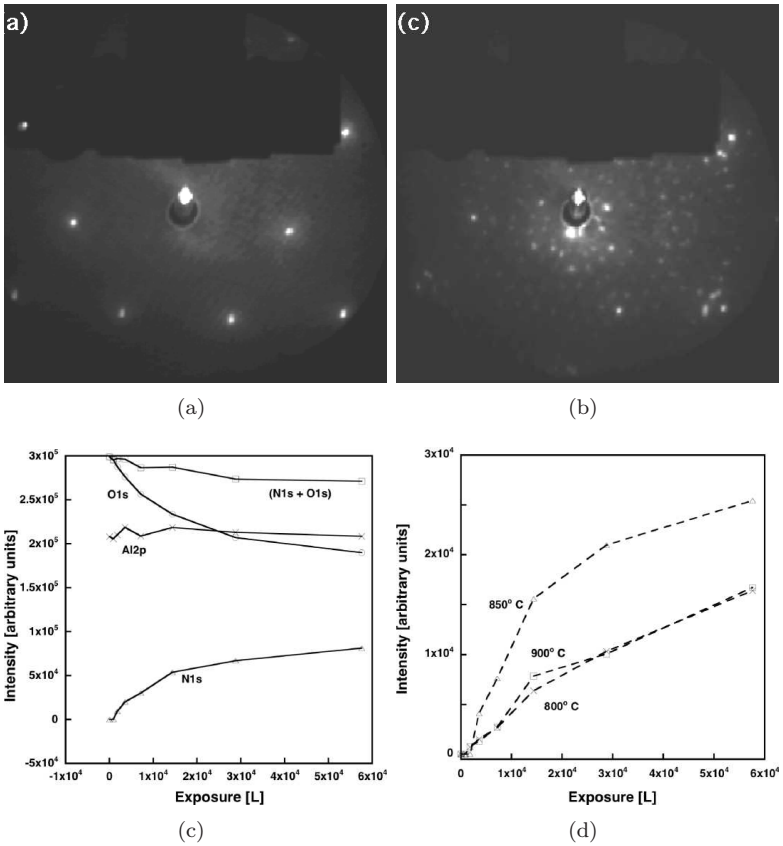

Figure 4.1. a) LEED image of a unreconstructed α-$Al_2O_3(0001)$ substrate. b) LEED image of reconstructed substrate after high temperature annealing. c)N1s, O1s, and Al2p peak intensities as a function of exposure at 850 °C on reconstructed substrate d) Integrated nitrogen XPS intensity as a function of deposited ammonia for different substrate temperatures on unreconstructed substrate.

4.2 Paper [P2]

As discussed in paper [P1], the surface reconstruction of the sapphire surface plays an important role in the nitration process and thus in the initial stages of the GaN epitaxial growth. However for a successful epitaxial layer to form on a substrate it is also absolutely crucial that the substrate is atomically smooth with step edges or terraces to form suitable nucleation sites for the growth to take place. In paper [P2] the effect of high temperature annealing on sapphire substrates was investigated using AFM, triple-axis high resolution X-ray diffraction (THRXRD), SE and *in citu* RHEED.

The AFM study shows that the sapphire surface develops differently depending on annealing time and on chemical environment in which the annealing takes place. A high quality atomically flat surface with step edges is achieved after thermal cleaning in H_2 ambient and subsequent annealing at 1300 °C in O_2 for 11 hours (see figure 4.2(a)). The THRXRD analysis indicate that the crystalline quality of the substrate improves upon annealing and that the lattice parameters could also be affected. No shift in absorption peak position was observed above and near the band-gap energy of α-$Al_2O_3(0001)$ substrate after annealing. The RHEED images of the substrate before and after high temperature annealing show some kind of reconstruction forming after the annealing (see figure 4.2(b)). Comparing this to the conclusions from the LEED experiments in paper 1, it might be tempting to conclude that this reconstruction is indeed the observed $(\sqrt{31} \times \sqrt{31})R \pm 9°$ from that study but that was never confirmed.

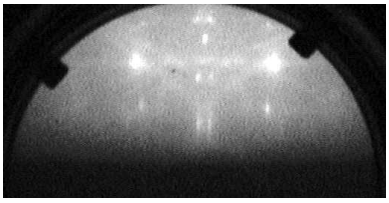

(a)

(b)

Figure 4.2. a) RHEED and b) AFM images of α-Al_2O_3(0001) substrate after few hours annealing in O_2.

4.3 Paper [P3]

The purpose of our experiments was to investigate the effect adsorption and subsequent desorption of indium has on the surface quality of sputtered GaN. As mentioned in the introduction, there are indications that indium acts as surfactant in GaN growth and helps rearrange the atoms in such a way that it results in a higher crystal quality and better surface morphology [6, 7, 8]. During GaN sputtering, which is often used as cleaning procedure in order to obtain well defined and ordered GaN surface, metallic Ga tends to form in small amount on the surface. The amount of metallic gallium depends on the angle of incident of the ion-beam as well as on the kinetic energy of the ions [29, 30, 31]. This metallic part can compose a problem and can be difficult to remove. By depositing a small amount of indium on to the sputtered GaN surface and subsequently anneal it we found that it was possible to remove both the indium and the metallic gallium leaving behind a clean, well ordered GaN crystal. The experiments were carried out at Maxlab, Sweden at beamlines 41 and D1011 in 2006. The results from beamline 41 showed that soft sputtering of GaN, followed by a small deposition of indium and subsequent annealing totally removed the metallic gallium from the surface.

Figure 4.3 shows the development of the Ga3d and In4d peaks is at various stages during the experiment. The sample was introduced into the XPS chamber and subsequently soft sputtered (acceleration voltage at 500V) until most of the carbon had been removed from the surface. After sputtering, a metallic gallium part is clearly present at lower binding energy to the gallium peak corresponding to gallium in GaN compound. By depositing small amount of indium and subsequently annealing, the indium together with the metallic gallium part are totally removed, leaving behind a single Ga3d component representing gallium in GaN compound.

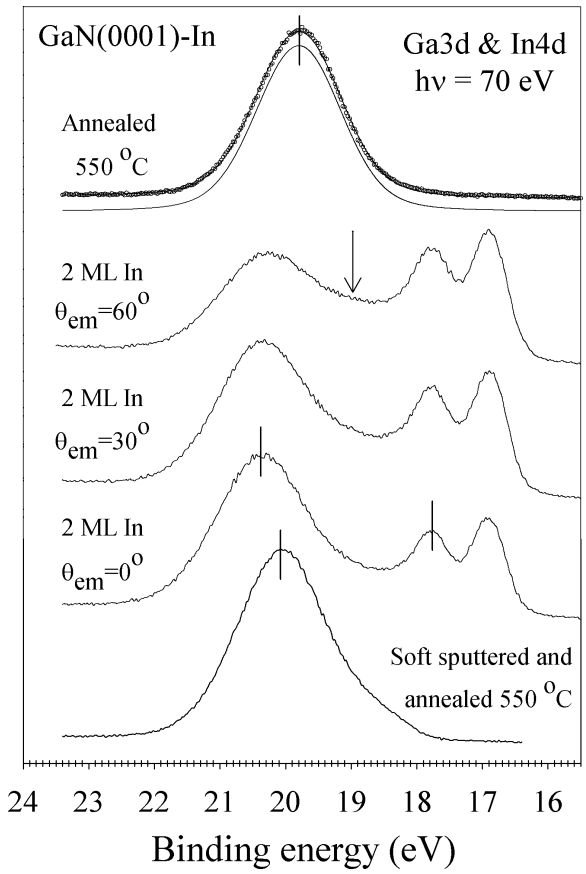

Figure 4.3. Development of the Ga3d peak. a) After soft sputtering and annealing. b) After 3-4 Åindium deposition measured at $\theta = 0°$. c) The same as b) but measured at $\theta = 30°$ d) The same as b) but measured at $\theta = 60°$ e) After 2 hours annealing at temperatures ranging from 150 to 540 °C.

Experiments using hard sputtering however seemed to incorporate indium into the substrate and thus did not help in improving the GaN layer. Soft sputtering seams to be the key in achieving the desired behaviour of desorption of both metallic indium and gallium after annealing.

Bibliography

[1] K. Butcher and T. Tansley, "InN, latest development and a review of the band-gap controversy," *Superlattices and Microstructures*, vol. 38, no. 1, pp. 1–37, 2005.

[2] J. H. Edgar, S. Strite, I. Akasaki, H. Amano, and C. Wetzel, eds., *Properties, processing and application of Gallium Nitride and Related Semiconductors*. INSPEC, 1999.

[3] I. J. Pankove and D. T. Moustakas, eds., *Gallium Nitride (GaN) I, Semiconductor and semimetals*, vol. 50. Academic Press, 1998.

[4] I. J. Pankove and D. T. Moustakas, eds., *Gallium Nitride (GaN) II, Semiconductor and semimetals*, vol. 57. Academic Press, 1998.

[5] S. Nakamura, S. Pearton, and G. Fasol, *The Blue Laser Diode*. Springer, 2nd ed., 1997.

[6] Z. Feng, H. Yang, S. Zhang, L. Duan, H. Wang, and Y. Wang, "Effect on the optical properties and surface morphology of cubic gan grown by metalorganic chemical vapor deposition using isoelectronic indium surfactant doping," *Journal of Crystal Growth*, vol. 235, pp. 207–211, 2002.

[7] W. Fong, C. Zhu, B. Leung, C. Surya, B. Sundaravel, E. Luo, J. Xu, and I. Wilson, "Characterizations of gan films grown with indium surfactant by rf-plasma assisted molecular beam epitaxy," *Microelectronics Reliability*, vol. 42, pp. 1179–1184, 2002.

[8] F. Widmann, B. Daudin, G. Feuillet, N. Pelekanos, and J. L. Rouviere, "Improved quality gan grown by molecular beam epitaxy using in as a surfactant," *Applied Physics Letters*, vol. 73, no. 18, pp. 2642–2644, 1998.

[9] C. Kittel, *Introduction to solid state physics*. USA: John Wiley & sons, 1986.

[10] R. F. Pierret, *Advanced Semiconductor Fundamentals*. Upper Saddle River, New Jersey 07458: Prentice Hall., 2nd ed., 2003.

[11] N. W. Ashcroft and N. D. Mermin, *Solid State Physics*. Thomsons Learnings, Inc., 1976.

[12] M. S. Rogalski and S. B. Palmer, *Solid State Physics*. Gordon and Breach Science Publishers, 2000.

[13] H. Luth, *Solid Surfaces, Interfaces and Thin Films*. Germany: Springer-Verlag Berlin Heidelberg, 4th ed., 2001.

[14] J. Toofan and P.R.Watson, "The termination of the α- Al_2O_3 (0001) surface: a LEED crystallography determination," *Surface Science*, vol. 401, pp. 162–172, 1998.

[15] E. A. Soares, M. A. V. Hove, C. F. Walters, and K. F. McCarty, "Structure of the α-Al_2O_3 (0001) surface from low-energy electron diffraction: Al termination and evidence for anomalously large thermal vibrations," *Physical Review B*, vol. 65(195405), pp. 1–13, 2002.

[16] Y. Takeda and M. Tabuchi, "Sapphire substrates for growth of GaN and related compouns," in *Properties, processing and application of Gallium Nitride and Related Semiconductors* (J. H. Edgar and S. Strite and I. Akasaki and H. Amano and C. Wetzel, ed.), pp. 381–385, London, UK: INSPEC, 1998.

[17] T. M. French and G. A. Somorjai, "Composition and Surface Structure of the (0001) Face of α-Alumina by Low-Energy Electron Diffraction," *Journal of Physical Chemistry*, vol. 74(12), pp. 2489–2495, 1970.

[18] K. G. Saw, "Surface reconstruction of alpha-(0001) sapphire: An afm, xps, aes and eels investigation," *Journal of Materials Science*, vol. 39, pp. 2911–2914, 2004.

[19] P. S. P. Wei and A. W. Smith, "Structure of the (0001) Surface of α-Alumina," *Journal of Vacuum Science and Technology*, vol. 9(4), pp. 1209–1213, 1972.

[20] D. L. Smith, *Thin film deposition, Principles and practice*. USA: McGraw-Hill Inc., 1995.

[21] L. T. Romano, "General remarks on extended defects in gan and related materials," in *Properties, processing and application of Gallium Nitride and Related Semiconductors* (J. H. Edgar, S. Strite, I. Akasaki, H. Amano, and C. Wetzel, eds.), pp. 209 –212, London, UK: INSPEC, 1998.

[22] C. Kisielowksy, "Stain in GaN Thin Films and Heterostructures," in *Gallium Nitride (GaN) II* (Jacques I. Pankove and Theodore D. Moustakas, ed.), pp. 275–317, USA: Academic Press, 1999.

[23] M. Seah, "Quantification of AES and XPS," in *Practical Surface Analysis* (D. Briggs and M. Seah, eds.), pp. 181 – 216, New York: John Wiley & Sons, 1983.

[24] D. Briggs and J. T. Grant, *Surface Analysis by Auger and X-ray Photoelectron Spectroscopy.* Chichester: Eds., IM Publications, 2003.

[25] D. Briggs, *Handbook of X-ray and Ultraviolet Photoelectron Spectroscopy.* Heyden and Son, 1977.

[26] K. Siegbahn, C. Nordling, A. Fahlman, R. Nordberg, and B. Lindberg, *ESCA: Atomic, Molecular and Solid State Structure by means of Electron Specroscopy.* Uppsala, Sweden: Almqvist and Wiksells, 1967.

[27] A. Ichimiya and P. I. Cohen, *Reflection high-energy electron diffraction.* Cambridge University Press, 2004.

[28] F. Giessibl and C. Quate, "Exploring the nanoworld with atomic force microscopy," *Physics Today*, vol. 59, no. 12, p. 44, 2006.

[29] M. Petravic, V. A. Coleman, K. jeong Kim, B. Kim, and G. Li, "Defect acceptor and donor in ion-bombarded gan," *Journal of Vacuum Science and Technology*, vol. 23, no. 5, pp. 1340–1345, 2005.

[30] M. Petravic, P. N. K. Deenapanray, V. A. Coleman, K. jeong Kim, B. Kim, and G. Li, "Core-level photoemission and near-edge x-ray absorption fine-structure studies of gan surface under low-energy ion bombardment," *Journal of Applied Physics*, vol. 95, pp. 5487–5493, 2004.

[31] J. Kovac and A. Zalar, "Surface composition changes in gan induced by argon ion bombardment," *Surface and Interface Analysis*, vol. 34, pp. 253–256, 2002.